

Characterization of the Hamamatsu R14374 and HZC Photomultiplier tubes for the Hyper-Kamiokande experiment

immediate

August 16, 2021

1 Introduction

Hyper-Kamiokande (HK), a 260 kton water Cherenkov detector to be built in Japan, is the next generation of neutrino observatory under-construction in Japan. Figure 1 presents a schematic view of the HK detector. As Super-Kamiokande [1] (SK), HK aims for a world-leading sensitivity in a broad physics program including nucleon decay, solar and supernovae neutrinos, as well as determination of the neutrino mass hierarchy and leptonic CP violation. For this purpose, HK aims to observe neutrinos from astronomical, atmospheric or human-made sources ranging from few MeV to several hundreds of TeV.

Hyper-Kamiokande (ICRR-Univ. Tokyo)



Figure 1: Schematic view of the Hyper-Kamiokande far detector and J-PARC neutrino beam.

In particular, for the determination of a potential leptonic CP violation, the HK experiment will rely on the neutrino beam produced in J-PARC, located 295 km away from HK on the East coast of Japan. In J-PARC, a very pure beam of muon neutrinos (resp. anti-neutrinos) is produced and oriented 2.5° away from the direction of HK, where muon neutrino (resp. anti-neutrino) disappearance and electron neutrino (resp. anti-neutrino) appearance can be observed. HK will rely on the same complex of near detectors than the T2K experiment [2], ND280, located 280 m away from the neutrino production point, in order to constraint the neutrino beam before oscillation and henceforth reduce the systematic uncertainties down to 4% [3]. However, in order to maximize the probability to exclude CP conservation and measure the δ_{CP} parameter with high-precision, an additional reduction of the systematic uncertainty is necessary for HK. Consequently, the HK collaboration is planning to install an additional near detector, the Intermediate Water Cherenkov Detector (IWCD). The IWCD (figure 2) will be a 12 m high and 10 m diameter water tank installed 750 m away from the neutrino production point

on the beamline from J-PARC to HK. It will complete the ND280 detectors in order to reduce the systematic uncertainty on the neutrino flux, cross-section and detector model below 3%. To reach this performance, the IWCD aims for a $\leq 1\%$ detector uncertainty. To achieve this goal in spite of its reduced size compared to HK, the IWCD should rely on a photo-sensors with a higher time and spatial resolution than used in the HK far detector: the multi-PMT modules (mPMTs).

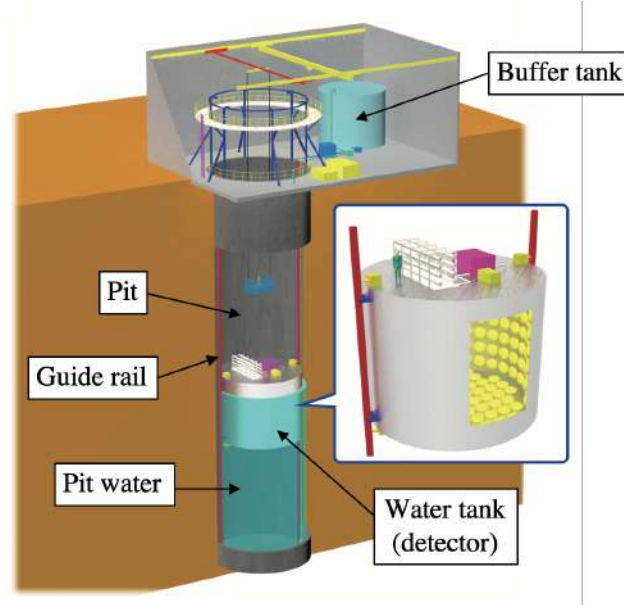


Figure 2: Schematic view of the Intermediate Water Cherenkov Detector (IWCD).

A mPMT, shown on figure 3, is an optical module based on a pressure vessel instrumented with 19 3" diameter photo-sensors, readout electronics and power. It offers several potential advantages compared to HK 20" PMTs, such as increased spatial granularity, reduced dark rate, weaker sensitivity to Earth's magnetic field, improved timing resolution and directional information with an almost isotropic field of view. For this reason, these photo-sensors are not only considered as primary candidates for the IWCD, but also as a complement to the 20" PMTs for the HK far detector.

Several options are considered for the individual 3" photo-sensors constituting these mPMTs. This paper aims

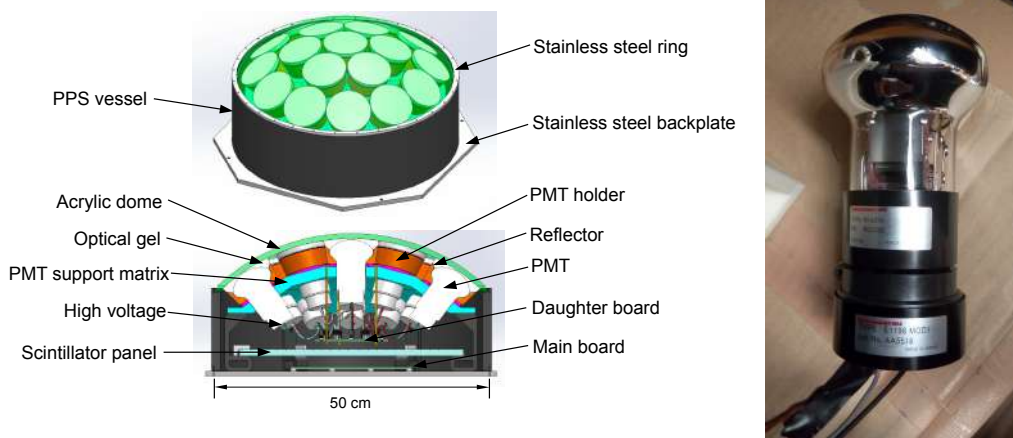


Figure 3: Schematic view of the mPMT (left). The Hamamatsu R14374 3" PMT (right).

to summarize the measured characteristics and performances of one candidate PMT: the Hamamatsu R14374 (figure 3).

2 Measurements of the PMT gain, Peak-to-Valley ratio and time response using a uniform light source

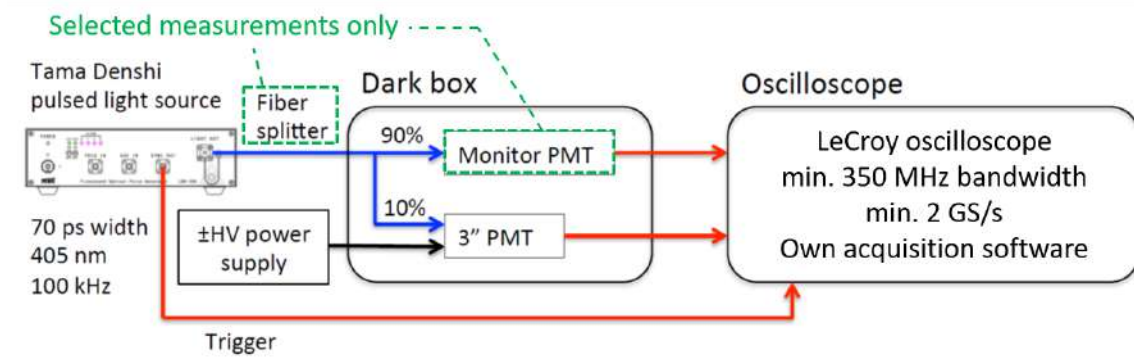


Figure 4: Schematic of the setup used for characterisation of 3" photomultipliers.

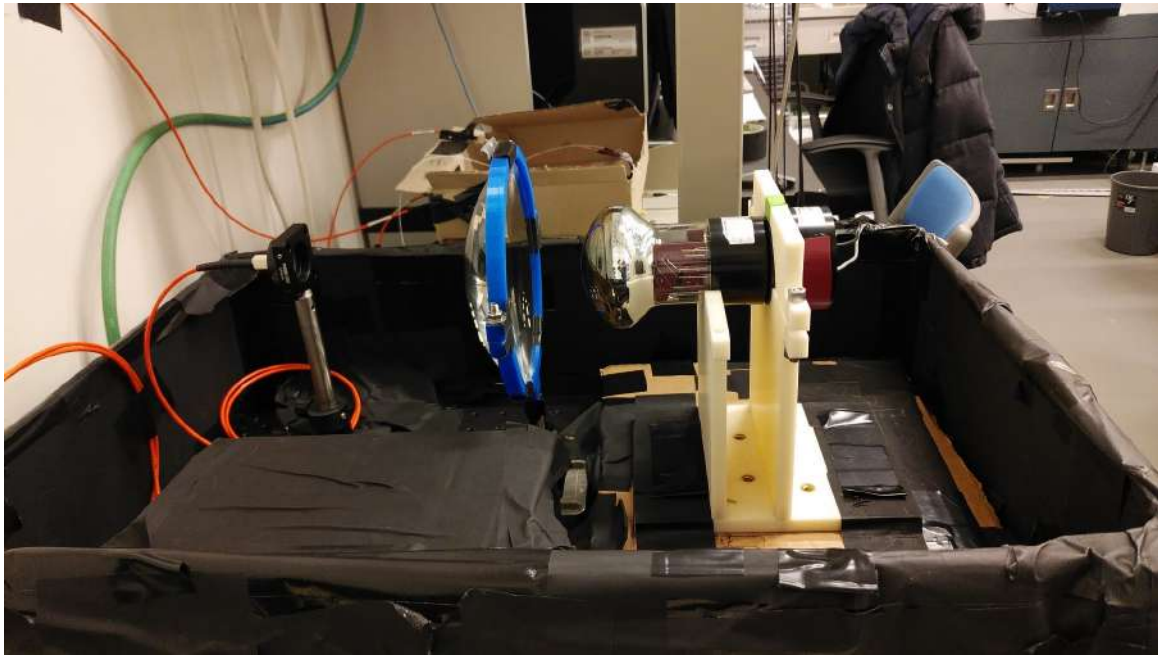


Figure 5: Picture of the test bench used for gain, efficiency and TTS measurements.

Most of the gain and timing resolution measurements of the new PMTs were done using a 402 nm laser diode pulsed with a generator and a waveform digitizer or a fast 2 GS/s oscilloscope (Fig. 4). The laser diode signal is split by a 1:9 fiber splitter which are respectively illuminating the 3" tested PMT and a Hamamatsu ?? monitor PMT. The monitor PMT is used to identify possible timing jitter of the light source, as well as to monitor the time stability of the source light intensity. The light source output dedicated to the 3" PMT illumination is collimated by a diffuser and a 14.05 cm (5.53") diameter lens in order to obtain a light pattern of parallel photons forming a 14.0 cm diameter disk centered on the PMT photocathode, as shown in Figure ??.

A peak-finding algorithm is run in order to identify multiple pulses from the PMT in one acquisition time window, and to set multiple triggers. When a trigger is found, the charge of the PMT is then integrated. The

charge spectrum was fit using a function f proposed in [?]:

$$f(x) = \mathcal{N} \times (S_{ped}(x) + S_{noise}(x) + S_1(x) + S_N(x)) \text{ with} \quad (1)$$

$$S_{ped}(x) = \frac{1-W}{\sqrt{2\pi}\sigma_0} \cdot e^{-0.5(\frac{x-Q_0}{\sigma_0})^2 - \mu} \quad (2)$$

$$S_{noise}(x) = \alpha W e^{-\alpha(x-Q_0)-\mu} \text{ if } x > Q_0, 0 \text{ otherwise} \quad (3)$$

$$S_1(x) = \frac{\mu^k e^{-\mu}}{\sqrt{2\pi}\sigma_1} \cdot e^{-0.5(\frac{x-Q_1-Q_{sh}}{\sigma_1})^2} \quad (4)$$

$$S_N(x) = \sum_{n=2}^{10} \frac{\mu^k e^{-\mu}}{n!} \frac{1}{\sqrt{2\pi}n\sigma_1} \cdot e^{-\frac{1}{2n}(\frac{x-nQ_1-Q_{sh}}{\sigma_1})^2} \quad (5)$$

where Q_0 , σ_0 , W , α , μ , σ_1 , Q_1 , Q_{sh} and \mathcal{N} are used as free parameters for the fit. Figure 6 shows an example of 3" PMT data set fit by this function f and confirms the fit quality. The gain of the PMT is defined as the

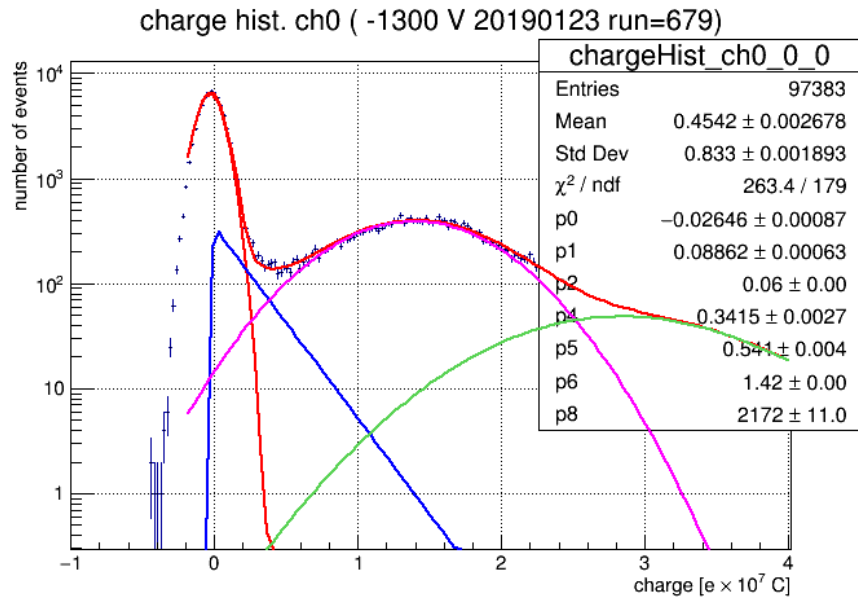


Figure 6: Charge distribution of the Hamamatsu R14374 PMT for laser diode signal close to 1 p.e., and fitted by the function f .

difference between the 1 p.e. and pedestal peak positions :

$$\mathcal{G} = Q_1 - Q_0 \quad (6)$$

and the peak-to-valley ratio as the difference between the 1 p.e. peak amplitude and the minimal amplitude points between the pedestal and 1 p.e. peak positions.

The timing of the pulses was obtained by either finding the half-height point of the leading edge of the PMT response, as shown in Figure 7. This definition was chosen in order to correct for time-walk effect which arises for signals with large charges. The pedestal subtraction needed for timing studies was performed using a histogram-based method. The output from the generator pulsing the laser diode is also analyzed, and a generator trigger timing is also defined similarly as for PMT (Figure 7). The Transit Time (TT) is defined as the time between the generator trigger and the PMT one. The TT distribution is fitted by the convolution of a gaussian and an exponential g defined as:

$$g(t) = \frac{\mathcal{K}}{2} e^{-\lambda(t-\mu)+0.5\lambda^2\sigma^2} \times [1 + \text{erf}(\frac{t-\mu-\lambda\sigma^2}{\sqrt{2\pi}})] \text{ with} \quad (7)$$

$$\text{erf}(t) = \frac{2}{\sqrt{\pi}} \int_0^t e^{-y^2} dy \quad (8)$$

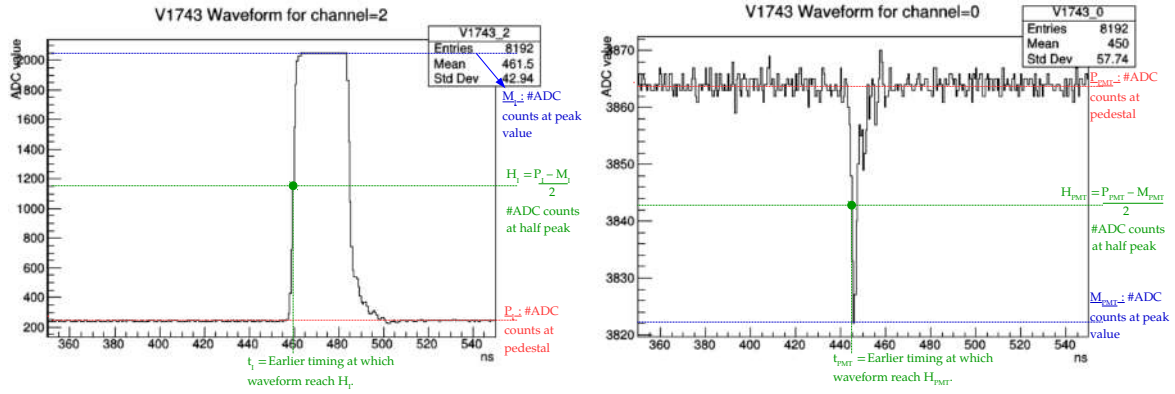


Figure 7: Description of the trigger time definition for the generator signal used as laser diode trigger (left) and the PMT signal (right)

Figure 8 shows an example of TT distributions fitted by the function above, and confirm the fit consistency. The Transit Time Spread (TTS) is defined as the Full Width at Half Maximum of the data distribution, and is used as a measure of the PMT timing resolution.

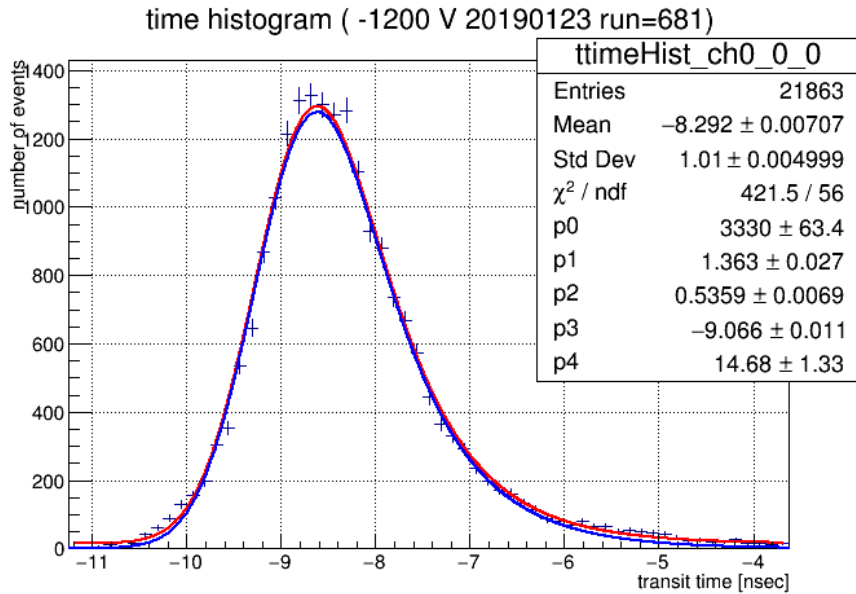


Figure 8: Transit Time distribution of the Hamamatsu R14374 PMT for laser diode signal close to 1 p.e., and fitted by the function g .

44

2.1 Results at the 1 p.e. level

The results are presented in Table 1 at a given gain of 10^6 . It confirms similar values of peak-to-valley ratio and timing resolution for a given gain, as well as the variability of the corresponding high-voltage depending on the PMT. The variation of the Hamamatsu R14374 PMT gain and peak-to-valley ratio as a function of the HV are shown on Fig. 9 for both positive and negative High-Voltage modes. The behaviour of the TTS as a function of the HV is indicated on Fig. 10.

2.2 Charge and timing response with respect to light intensity

The measurements presented so far has been established with a light source close to the 1 p.e. level. In this section, the behaviour of the charge and timing response with respect to the input charge is measured. The

PMT	HV	Gain	Peak-to-Valley	TTS
BC0035	-1170 V	$1 \cdot 10^6$	2.5	1.52 ns
	1171 V	1×10^6	2.5	1.56 ns
BC0038	1226 V	$1 \cdot 10^6$	2.3	1.63 ns
	1238 V	1×10^6	2.6	1.58 ns

Table 1: Gain, charge resolution and TTS measurements for Hamamatsu photomultipliers. The TTS measurements were made with a uniform light source illuminating the whole photocathode.

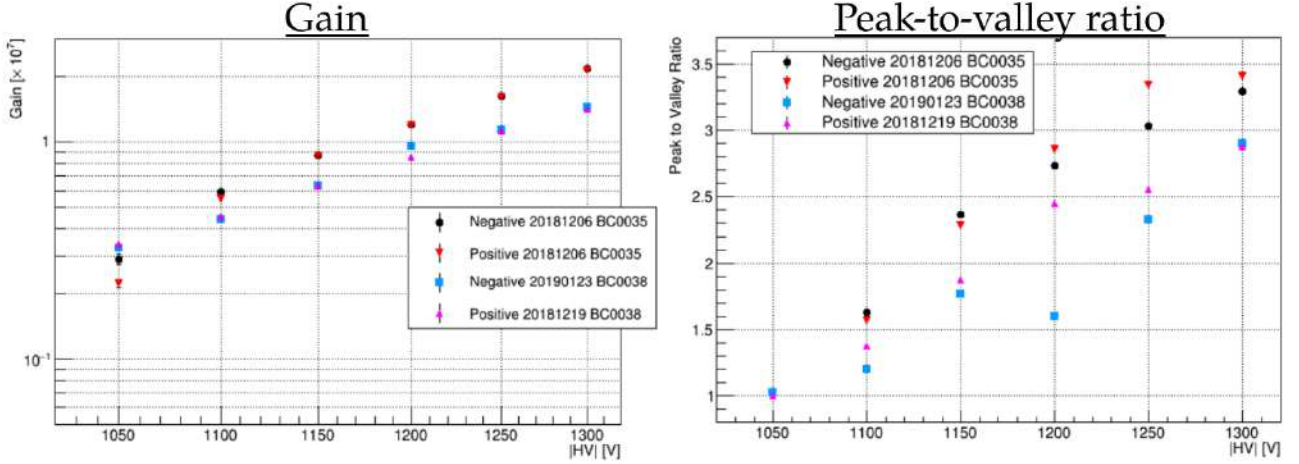


Figure 9: Gain (left) and Peak-To-Valley ratio (right) of the Hamamatsu R14374 as a function of the high-voltage, for 2 PMTs and in both positive and negative HV modes, at 25°C.

timing response has been measured with the very same setup as presented so far. The input charge is controlled by the monitor PMT, and varied from 1 to 5 p.e. Figure 10 shows the TTS variation with respect to the number of p.e., and shows that approximating the TTS variation as $1/\sqrt{p.e.}$ is reasonable.

In order to probe for possible calibration issues, the PMT output charge has been measured with respect to the input light on a considerably larger range than the TTS, namely from 1 to 10^4 p.e.. On such a large range, both the laser diode and the monitor PMT are expected to be highly non-linear, and the input light therefore requires to be controlled differently. For this reason, a different setup and methode was used for this measurement in order to guarantee an accurate measure of the input light intensity. The PMT is illuminated by two sources: a LED and a laser diode, as shown in Figure 11. The method used is to assume that the PMT has a linear response on a limited and narrow charge range. It is described below:

1. the LED intensity is set to a given value A while the laser diode is off. The PMT output charge $O(A)$ is measured.
2. the laser diode intensity is set to a given value B1 while the LED is off. The PMT output charge $O(B1)$ is measured.
3. the LED and laser diodes are simultaneously illuminating the PMT with intensities respectively set to A and B1. The PMT output charge $O(A+B1)$ is measured.
4. the PMT response is assumed to be linear between B1 and $A+B1$, and a linear interpolation is therefore performed between B1 and $A+B1$. The LED is off, and the laser diode intensity is increased so the output charge of the PMT reach the mid-point between B1 and $A+B1$, *i.e.* so that the output charge is $O(B1+A/2)$. The associated input light intensity, B2, is registered. In this way, the laser diode non-linearities are corrected using the assumption that the PMT response on a limited input light range is linear.
5. B2 replaces B1, and the steps are repeated from step 3.

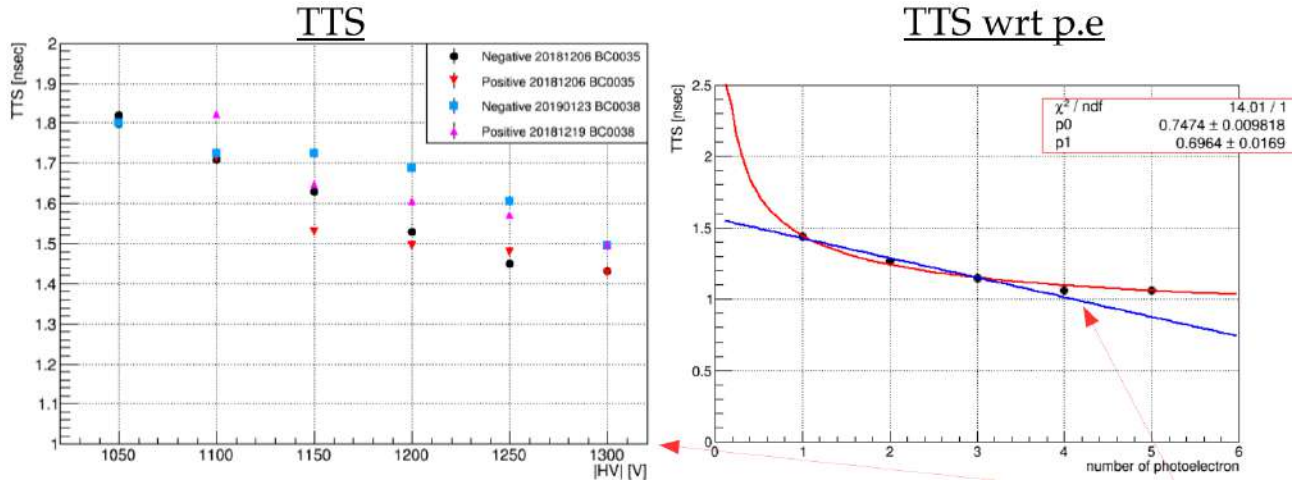


Figure 10: (Left) TTS of the Hamamatsu R14374 as a function of the high-voltage, for 2 PMTs and in both positive and negative HV modes, at 25°C. (Right) The TTS behaviour as a function of the detected charge is shown on the right, and has been fitted with a line (blue) and a function in $1/\sqrt{p.e.}$ (red).

78 The results are shown in Figure 12. They highlights that a deviation from $\pm 10\%$ to a linear response is guar-
79 anteed on the 1-400 p.e. range. Moreover, the PMT response as a function of the input charge shows that these
80 non-linearities slightly varies with respect to the PMT gain.

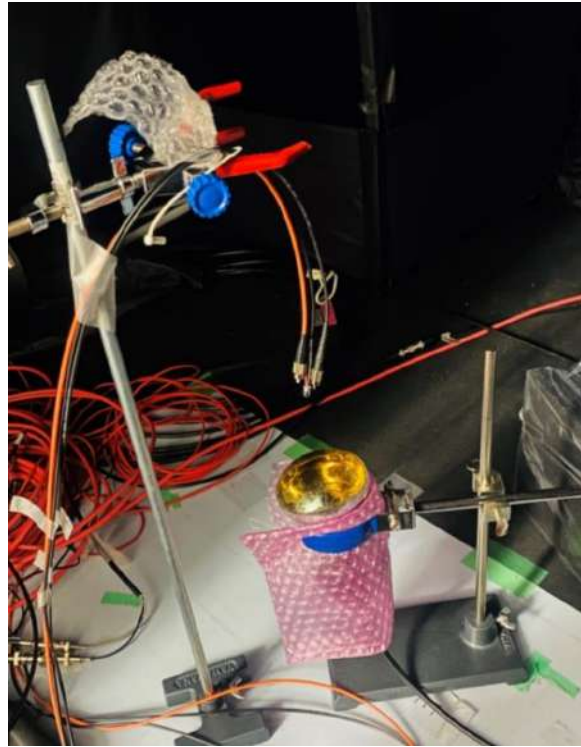


Figure 11: Picture of the setup used for the charge linearity measurements. The LED and laser diode illuminating the PMT are visible.

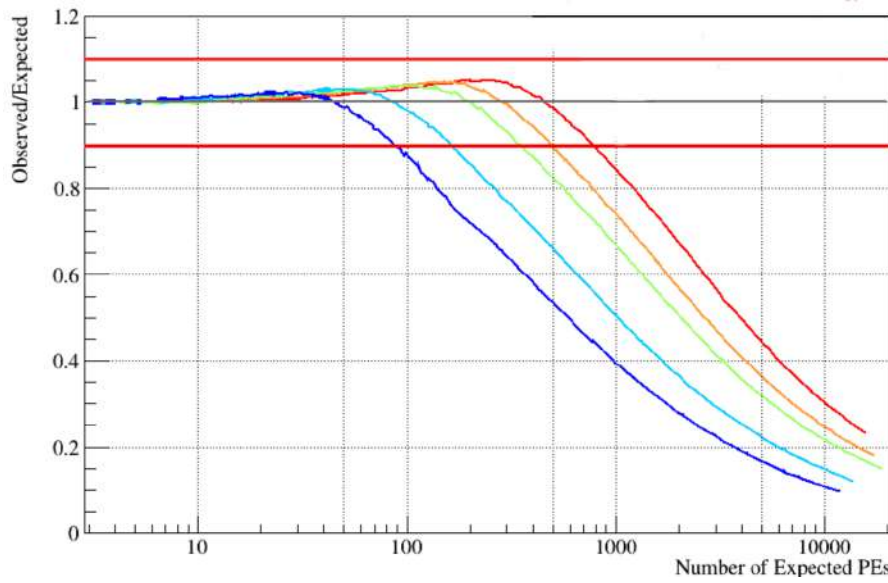


Figure 12: PMT output charge deviation to a linear response as a function of the input light. The PMT non linearities are measured for a high voltage (gain) of 1080 V (3.4×10^6) (red), 1180 V (5.6×10^6) (orange), 1280 V (8.3×10^6) (green), 1380 V (1.8×10^7) (cyan), 1480 V (3.3×10^7) (blue).

3 Position and angular dependency

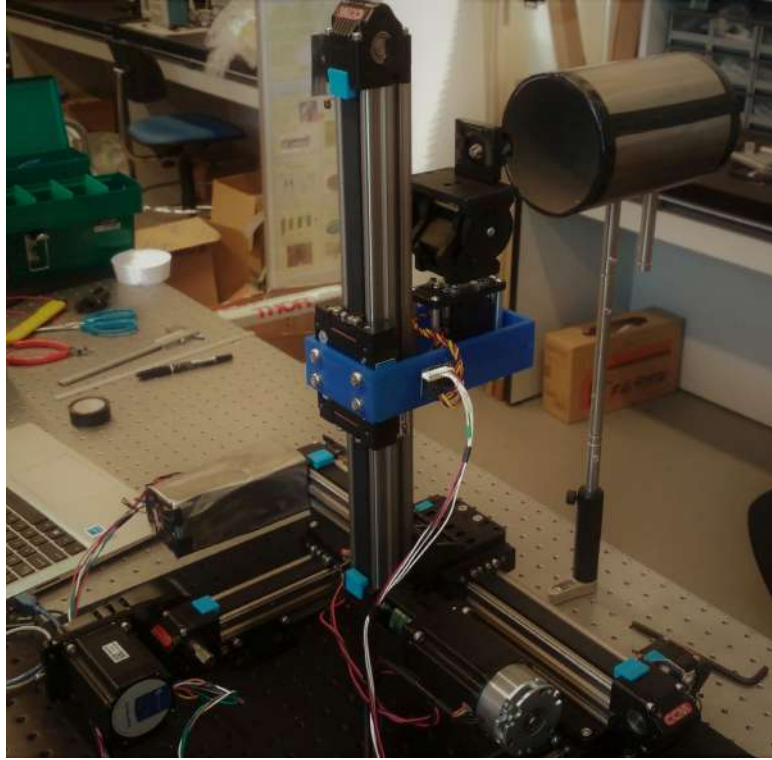


Figure 13: Setup for precise surface scans of 3" PMTs, which allows for variable angles of incidence of light over the entire photocathode.

Using the movable laser system which can illuminate a different position on the photocathode, efficiency, gain, TT, and TTS of the 3" PMTs as a function of the position on the photocathode were measured. The movable laser system consists of pan/tilt system stage and four linear modules with stepper motors: two along z -axis and the two others along x and y -axes. The laser fiber is mounted on the pan/tilt system stage. The schematic view of the movable laser system is shown in Fig.14. This system enables to illuminate various positions on the photocathode at various angles. The PMT is fixed in the tube covered with a mu-metal to eliminate the effect of the Earth's magnetic field.

In the position dependent measurement, the laser illuminated 306 points, 17 points in horizontal direction and 18 points in vertical direction on the photocathode at 5 mm intervals. The angle was kept parallel to the axis of the PMT. Two Hamamatsu R14374 PMTs were tested with both +1200 V and -1200 V. The efficiency at each point is presented in Fig. 15. The efficiency is uniform on most of the photocathode within $\pm 20\%$. There is no correlation between the efficiency and the arrow in Fig. 15, which shows the dynode orientation of the PMT. The arrow shows the direction from the first dynode to the second dynode. The result of the gain measurement is presented in Fig. 16. Gain is about 10% higher at the arrow head which corresponds to the second dynode side. There are also some correlation between the dynode orientation and the time response as shown in Fig. 17 and Fig. 18. TT tends to be about 10% smaller at the second dynode side while TTS shows the opposite trend. TTS is about 30% smaller at the first dynode side and about 20% larger at the second dynode side than that at the center. Consistent results were confirmed with another PMT. Each characteristic of both PMTs along x -axis is shown in Fig. 19 and Fig. 20.

To conclude the position measurement, efficiency is uniform within $\pm 10\%$ and is not correlated to the dynode orientation. On the contrary, gain and time response have some correlation to the dynode orientation. Therefore, the orientation of the dynode of each 3" PMT should be recorded when installing the multi-PMT modules.

Those characteristics depending on the incident angle of photons were also measured. Using the same setup as the position dependency tests, the performance of the two 3" PMTs (BC0035 and BC0038) was measured when the laser illuminated the center of the PMT at an angle of 0-75 degrees (Fig. 21). Then, the PMT was

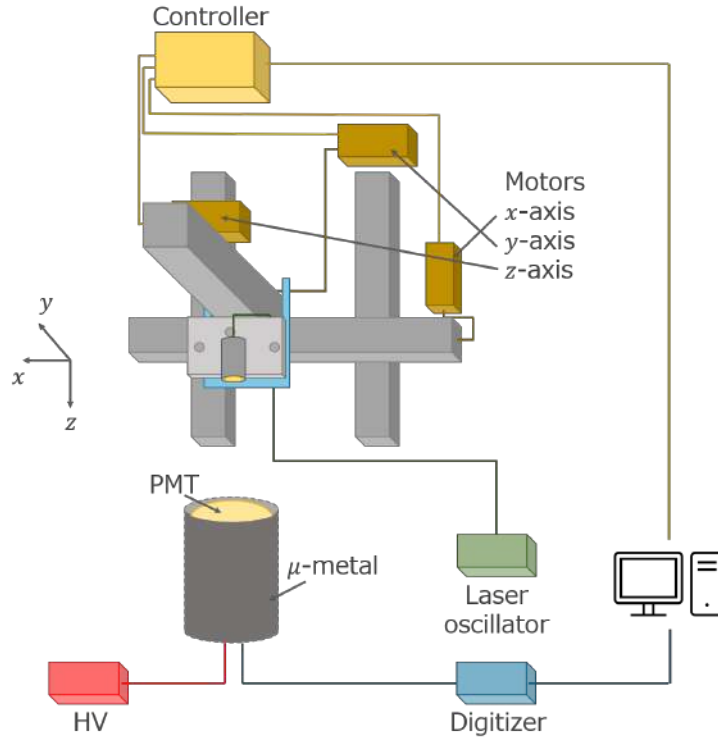


Figure 14: Schematic view of the movable laser system.

108 rotated 180 degrees around the axis and was measured again. The results are shown in Fig. 22 and Fig. 23.
 109 Consistent results were obtained with both PMTs. Efficiency drops rapidly when the incident angle is larger
 110 than 50 degrees. On the other hand, gain is uniform within $\pm 10\%$ regardless of the incident angle. In both
 111 PMTs, TT is uniform before rotation, but it shows a sudden drop of about 5% at around 60 degrees. One
 112 observes a slight difference between the TT before and after rotation for PMT illumination with a 0 degree
 113 angle. It is assumed to be a consequence of a possible shift between the light incident point and the PMT center
 114 (≤ 0.5 cm). The variation of trends between before and after the rotation indicates that it is due to the dynode
 115 structure. The effect of the dynode structure is also seen in TTS. While TTS is uniform within $\pm 5\%$ before
 116 rotation, TTS itself and the variation of TTS is larger after rotation; it maximize at around 60 degrees with both
 117 PMTs.

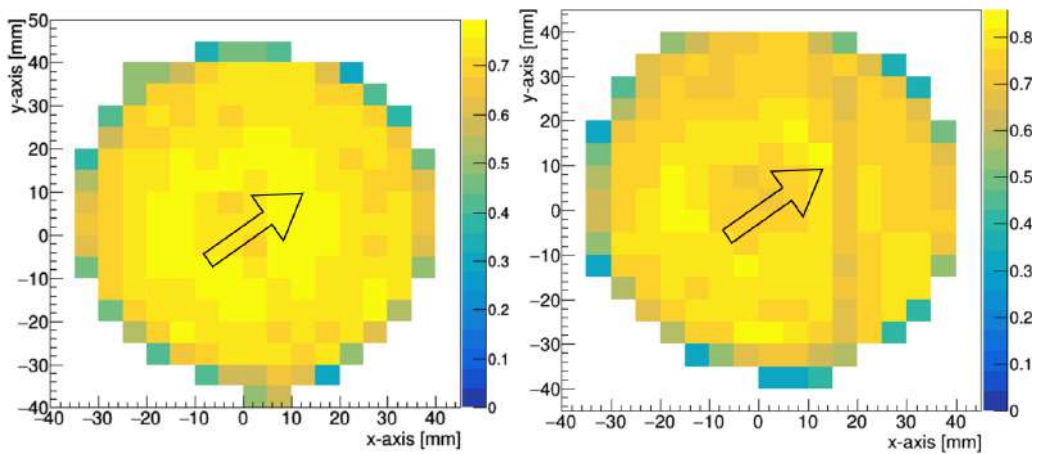


Figure 15: Position dependent efficiency of the PMT measured with +1200 V (left) and -1200 V (right).

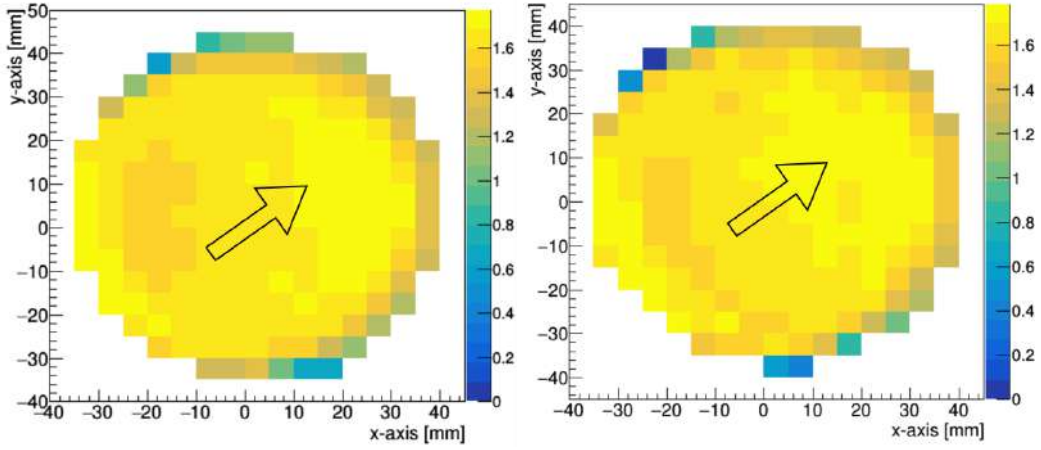


Figure 16: Position dependent gain of the PMT measured with +1200 V (left) and -1200 V (right).

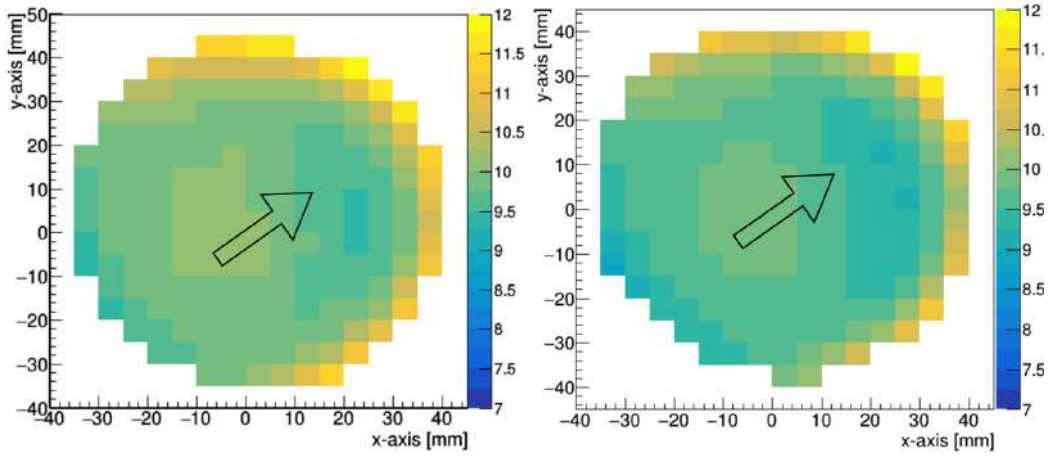


Figure 17: Position dependent TT of the PMT measured with +1200 V (left) and -1200 V (right).

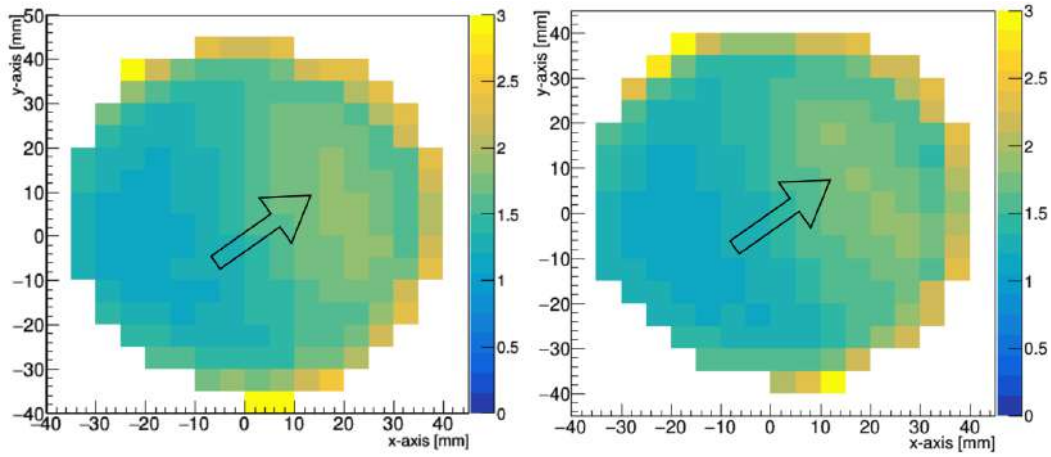


Figure 18: Position dependent TTS of the PMT measured with +1200 V (left) and -1200 V (right).

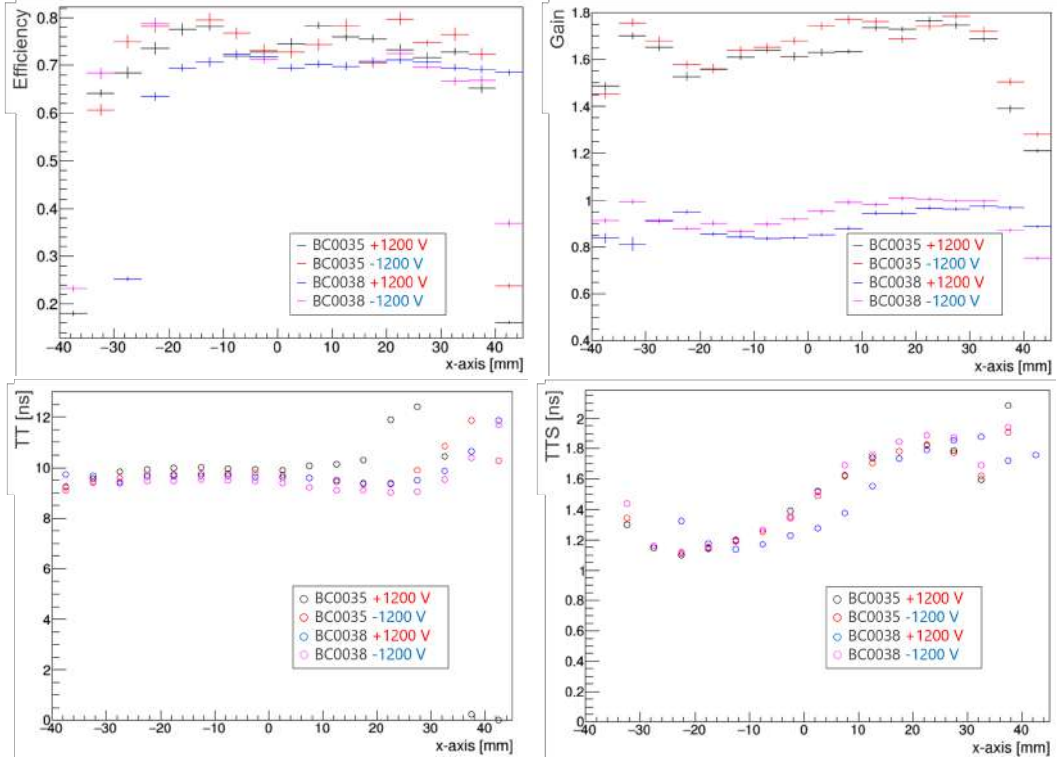


Figure 19: 1D plot of efficiency (top left), gain (top right), TT (bottom left) and TTS (bottom right) along x -axis. Measurements of two PMTs (BC0035 and BC0038) are overlaid.

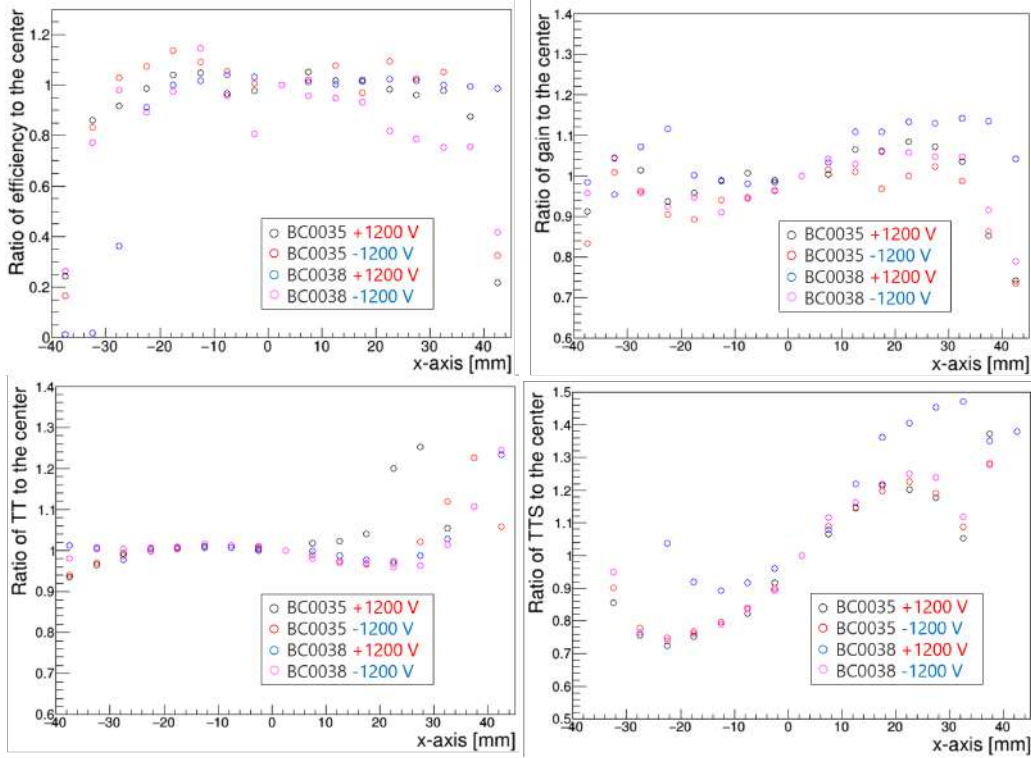


Figure 20: Ratio of efficiency (top left), gain (top right), TT (bottom left) and TTS (bottom right) to the center of the PMT along x -axis.

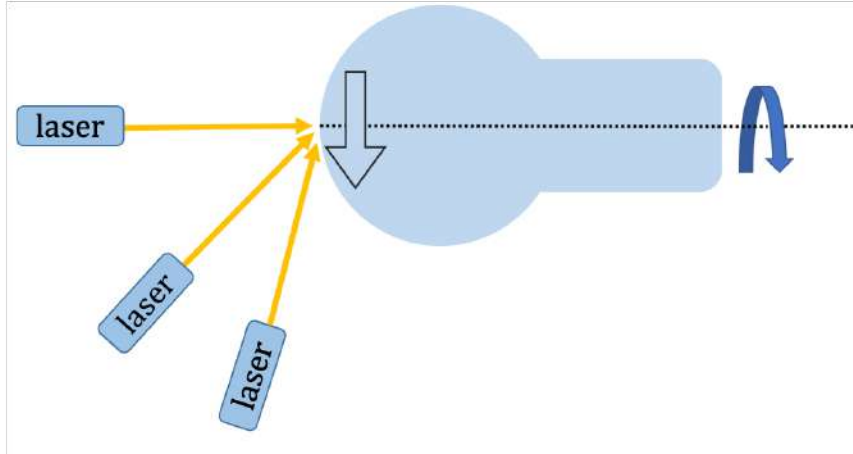


Figure 21: Configuration of the laser during the angle measurement. The black arrow shows the direction of the first dynode to the second dynode before rotation.

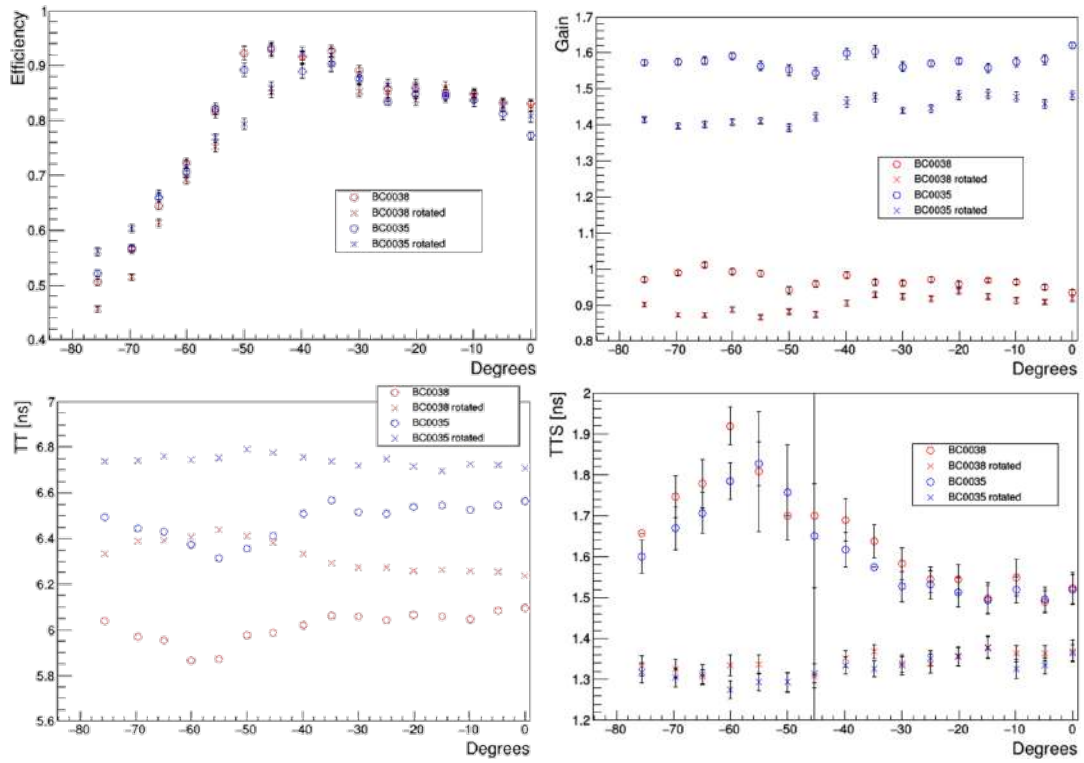


Figure 22: Angle dependent efficiency (top left), gain (top right), TT (bottom left) and TTS (bottom right) of PMT BC0035 and BC0038 before and after rotation.

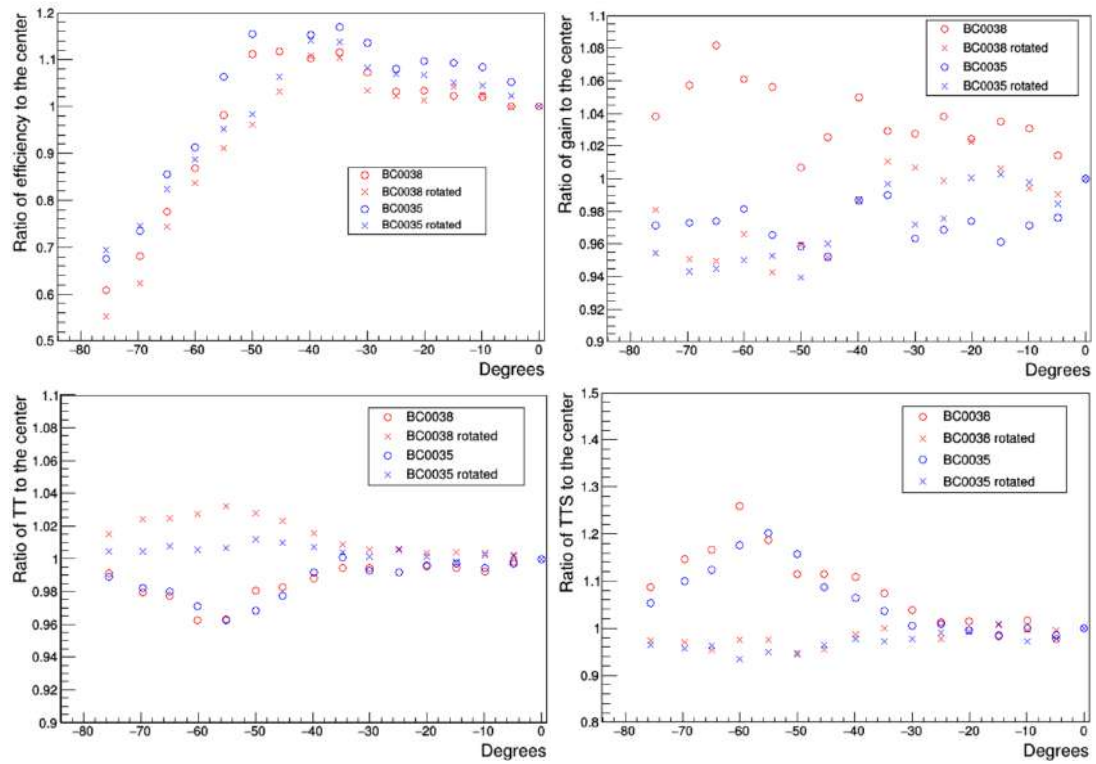


Figure 23: Ratio of angle dependent efficiency (top left), gain (top right), TT (bottom left) and TTS (bottom right) to the center of PMT BC0035 and BC0038 before and after rotation.

4 PMT magnetic field dependency

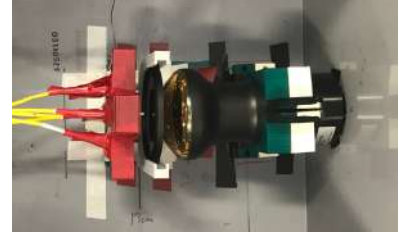
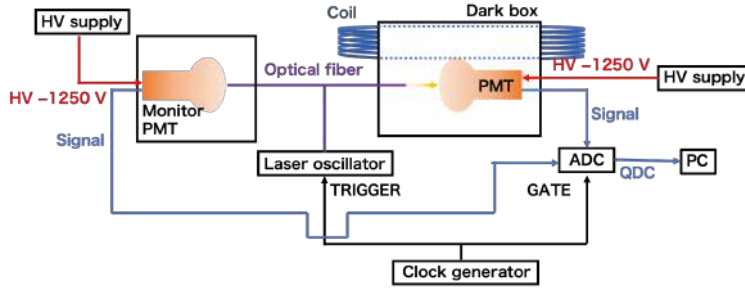


Figure 24: (Left) Schematics of the measurement setup of the 3" PMT with respect to B-field. (Right) fiber support structure with the 3" PMT.

The characteristics of PMTs are modified by the Earth's magnetic field. However, due to reduced drift length for electrons compared to 20" PMTs, this effect is expected to be considerably smaller for 3" PMTs. This section presents the relative gain and efficiency variations of the 3" PMTs with respect to magnetic field intensity and direction.

The measurement setup is shown in Figure 24 and is very similar to Section 2. The 402 nm laser light is divided by a divider which respectively illuminate the monitor PMT with more than 10 p.e. level intensity (see Section 2) and the 3" PMT with less than 1 p.e. intensity to test. The 3" PMT photocathode is illuminated at various points, shown in Figures 27 - 30, by the 5 mm diameter fiber spot. The dark box containing the 3" PMT is wrapped by a cylindrical coil which allow to generate a uniform magnetic field in the box in a single direction. The magnetic field direction, as well as the linear relation between the electric current applied to the coil and the magnetic field at the center of the dark box is calibrated using a Gauss meter, and shown in Figure 25.

First, the PMT response with respect to a magnetic field oriented in a perpendicular or parallel direction with respect to the laser photons and PMT photocathode has been performed. In this first measurement, the photon is aimed to the center of the photocathode and the monitor PMT is not used. The results are shown in Figure 26. About 20% variation in absolute efficiency is likely due to fiber connection, and this is the reason we employed monitor PMT for later measurement. The measurements demonstrate that the impact of magnetic field is negligible for magnetic field aligned with the photon direction. On one hand, it confirms our expectations, as the magnetic field is almost aligned with the direction of the electron emitted by the photocathode in this configuration. On the other hand, the PMT efficiency shows non-negligible variations even for values corresponding to the Earth magnetic field in case where the photons and magnetic field direction are perpendicular to each other. In the following subsections, additional measurements has been performed in this configuration in order to probe this effect in more details. The measurements have been divided into two categories depending if the magnetic field is oriented parallel to (Section 4.1) or perpendicularly (Section 4.2) to the dynode directions. Additionally to the PMT photocathode center, each configurations has been probed using 8 additional light injection point. The fiber position is moved accross the PMT photocathode using a support shown in Figure 21.

4.1 Magnetic field parallel to the dynodes

The measurements of the PMT efficiency and gain variation with respect to the magnetic field intensity and photon injection position on photocathode are shown in Figure 27 and Figure 28. In this configuration, the PMT gain varies by $\pm 7\%$ across the range of the Earth magnetic field, while the efficiency varies by 10%. The gain is especially reduced for the photon injection point on the top of the photocathode (blue and red in Figure 27).

4.2 Magnetic field perpendicular to the dynodes

The measurements of the PMT efficiency and gain variation with respect to the magnetic field intensity and photon injection position on photocathode are shown in Figure 29 and Figure 30. In this configuration, the

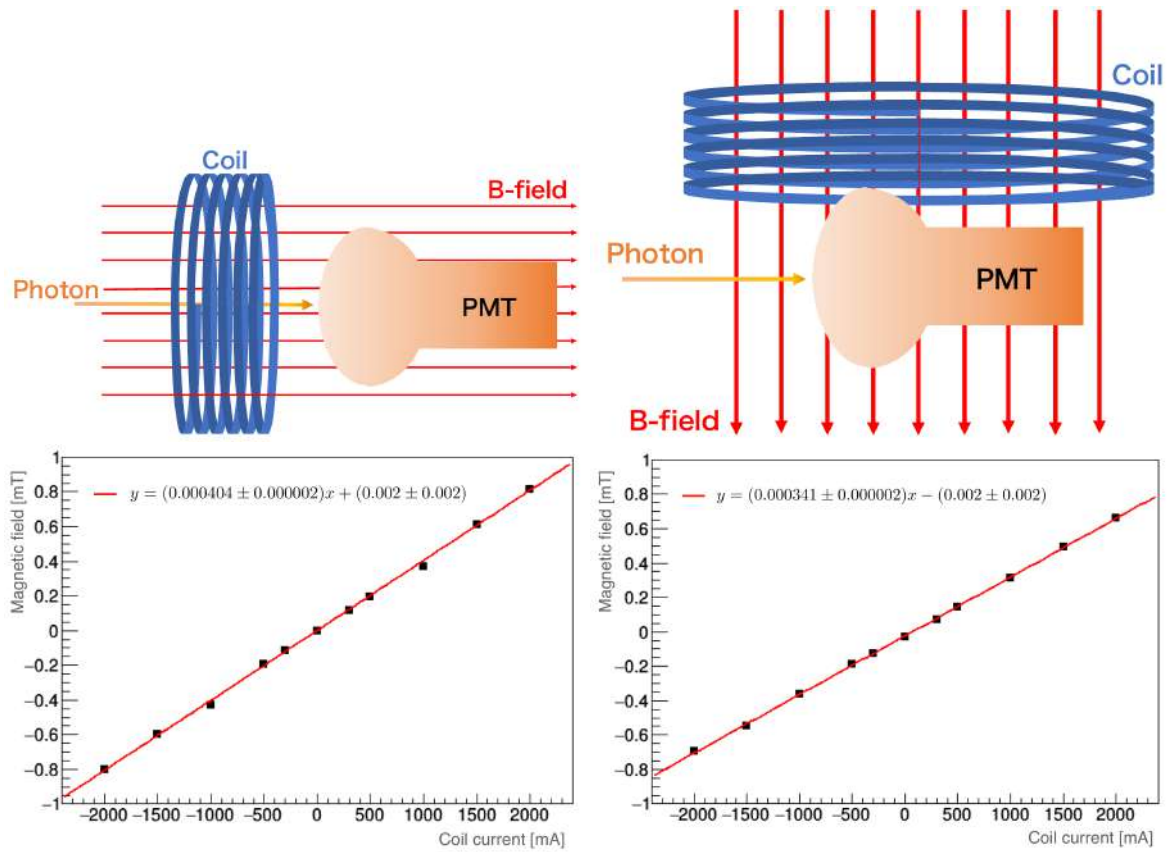


Figure 25: (Top) Schematics of the PMT and magnetic field when the magnetic field is perpendicular (left) or parallel (right) to the incident photon and photocathode surface. (Bottom) Variation of the magnetic field intensity at the center of the coil with respect to the electric current applied, when the magnetic field direction is perpendicular (left) or parallel (right) to the photocathode.

155 PMT gain varies by $\pm 13\%$ across the range of the Earth magnetic field, while the efficiency varies by 20%.

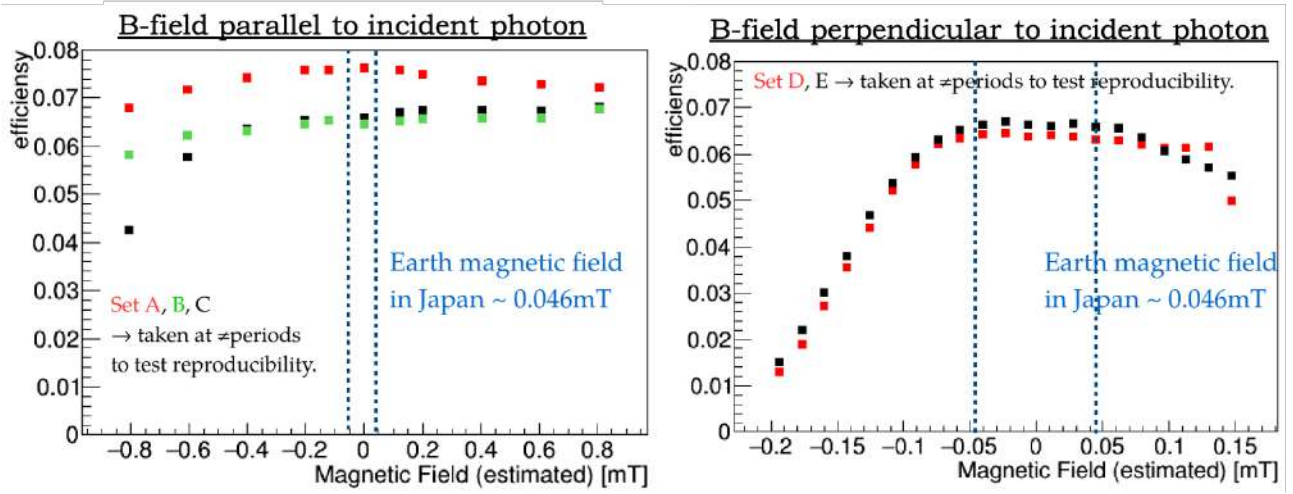


Figure 26: Results of the PMT R14374 relative efficiency variation as a function of the B-field intensity for a B-field parallel (left) and perpendicular (right) to the incident photon.

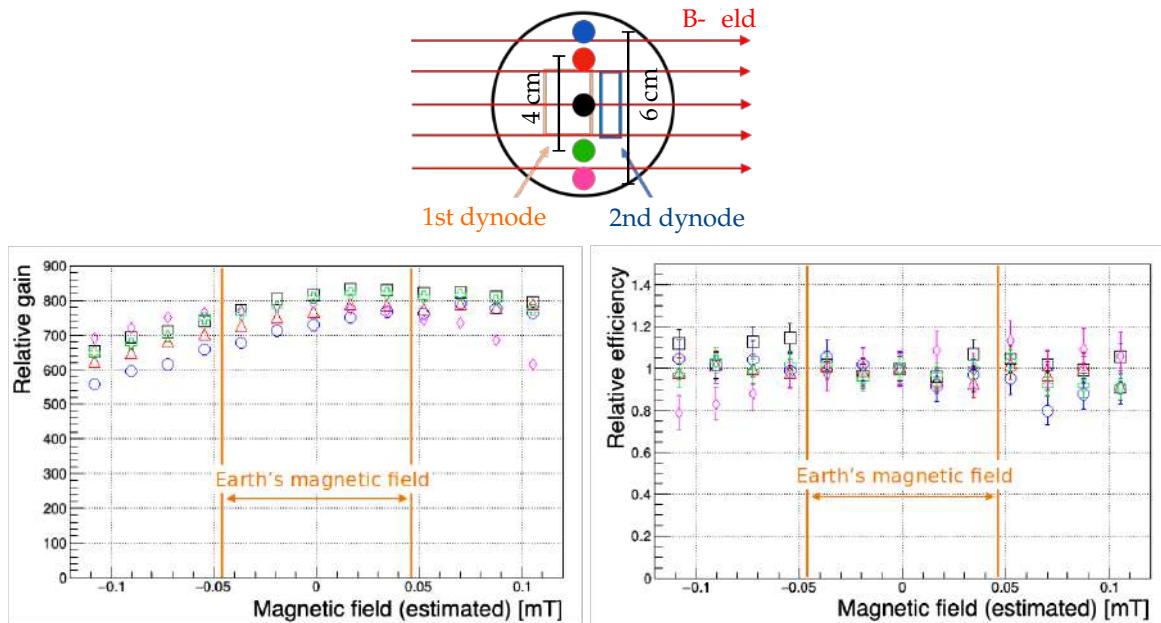


Figure 27: Measurements for magnetic field parallel to the first-to-second dynode direction, with laser moved vertically. (Top) Schematic of the B-field alignment with respect to PMT dynodes. The 5 laser injection points are shown. (Bottom) Relative gain (Left) and efficiency (Right) measurements with respect to B-field intensity. The colors represent the different measurements points indicated on the top plot.

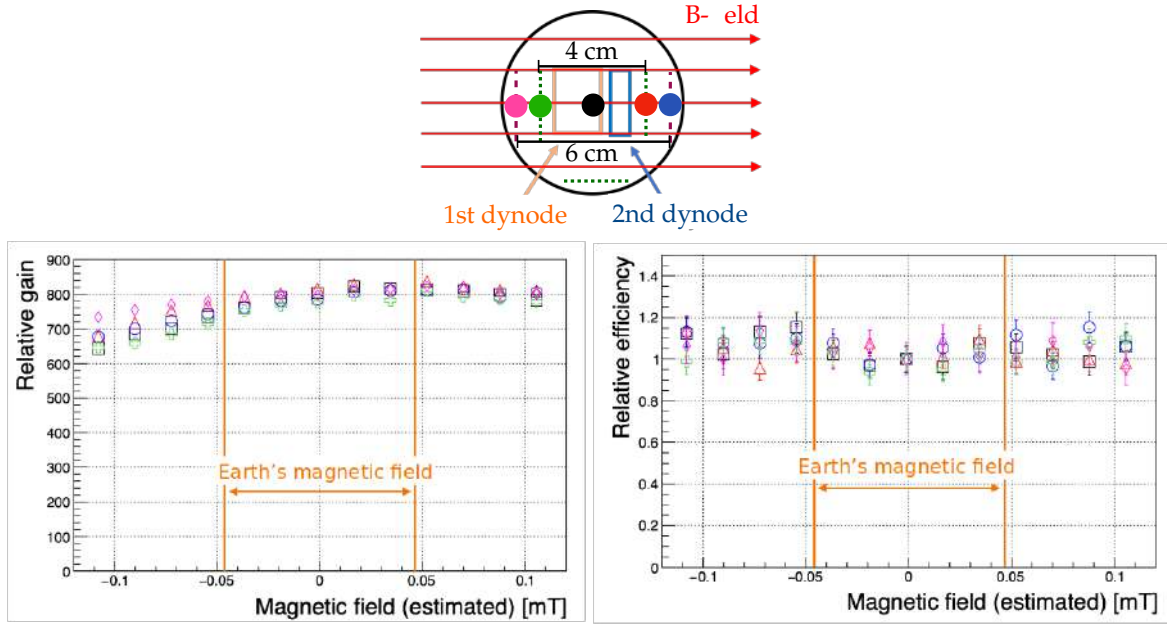


Figure 28: Measurements for magnetic field parallel to the first-to-second dynode direction, with laser moved horizontally. (Top) Schematic of the B-field alignment with respect to PMT dynodes. The 5 laser injection points are shown. (Bottom) Relative gain (Left) and efficiency (Right) measurements with respect to B-field intensity. The colors represents the different measurements points indicated on the top plot.

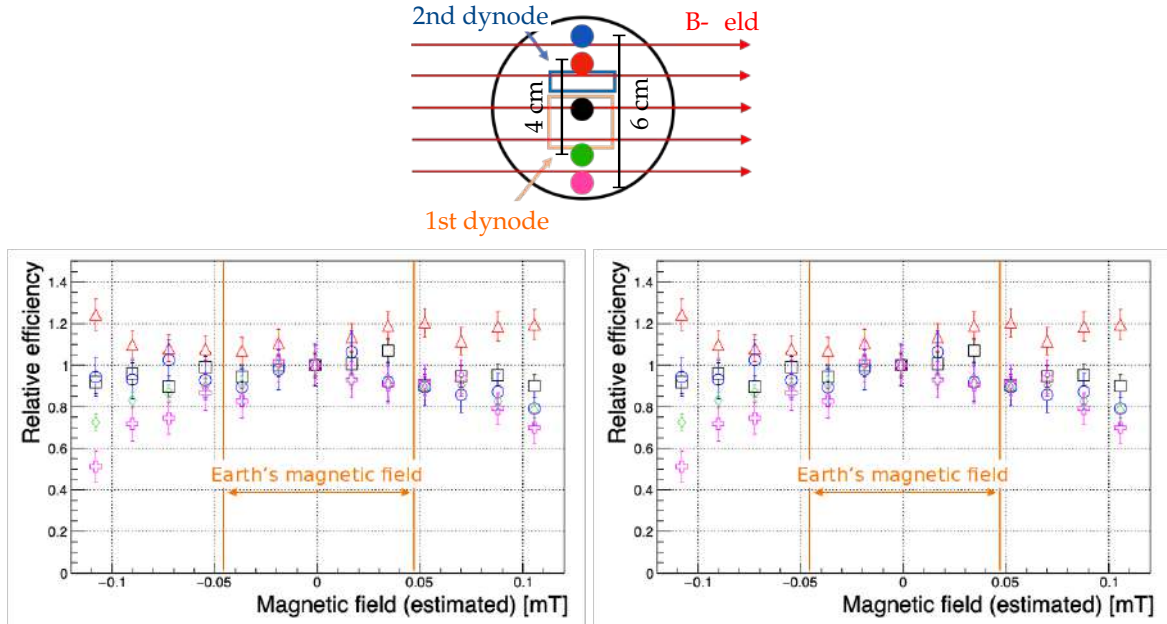


Figure 29: Measurements for magnetic field perpendicular to the first-to-second dynode direction, with laser moved vertically. (Top) Schematic of the B-field alignment with respect to PMT dynodes. The 5 laser injection points are shown. (Bottom) Relative gain (Left) and efficiency (Right) measurements with respect to B-field intensity. The colors represents the different measurements points indicated on the top plot.

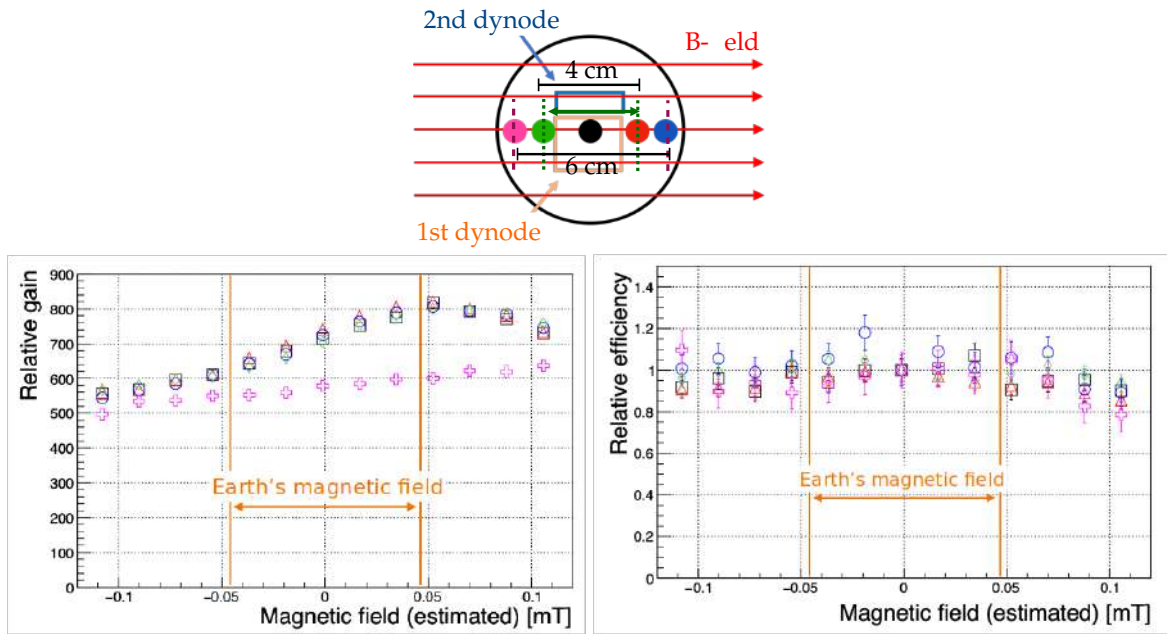


Figure 30: Measurements for magnetic field perpendicular to the first-to-second dynode direction, with laser moved horizontally. (Top) Schematic of the B-field alignment with respect to PMT dynodes. The 5 laser injection points are shown. (Bottom) Relative gain (Left) and efficiency (Right) measurements with respect to B-field intensity. The colors represents the different measurements points indicated on the top plot.

5 PMT Dark Rate Measurements

Dark rate measurements were performed using a temperature-stabilized dark box at different temperatures. For comparisons of different 3" PMTs, the gain has been set to 1×10^7 , which corresponds to a typical HV of 1250 V for the Hamamatsu R14374. The dark rate was measured 1 hour after the HV is applied as the most of the activation of the photocathode dying away after 40 minutes. Fig. 31 shows the results for the R14374 Hamamatsu PMTs with both positive and negative HV. At the temperature of water in the Super-Kamiokande detector (13°C), the dark rate was around 200 Hz for a threshold at 0.55 photoelectrons. One way of reducing the dark rate with a negative HV supply is to apply a metallic layer around the PMT, which is then covered by a dielectric layer to insulate the PMT surface (called HA-coating) and reduce the probability of accidental discharges [?]. Fig. 31 shows that a slightly lower dark rate of 150 Hz is observed at 13°C , although this is for comparison of only two PMTs. The 3" PMTs have still to be tested in water, a dielectric medium, where the results may differ between HA-coated and standard R14374 PMTs operating in negative and positive HV modes. A high electric field near the photocathode and glass envelope area can be problematic when objects at ground potential are placed close to the window, or more generally, near the glass envelope of the PMT. In such circumstances micro-discharges can occur. With the photocathode grounded this effect does not exist, as there

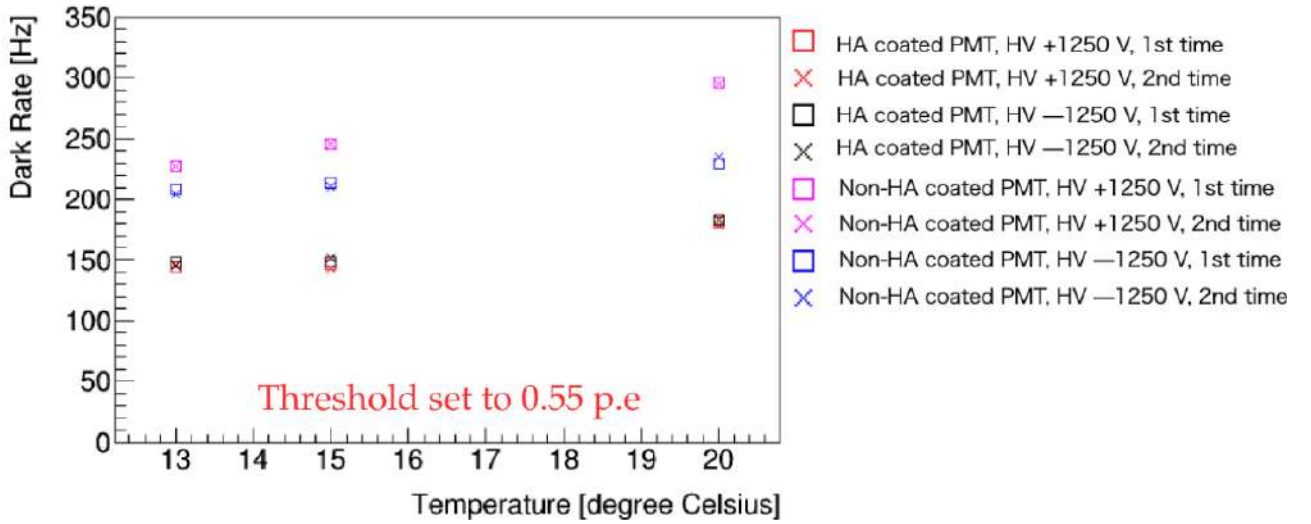


Figure 31: Dark rate of Hamamatsu R14374 operated at a gain of 1×10^7 in positive and negative HV modes for standard and HA-coated PMTs.

is no potential difference between the PMT and the outside structures. The drawback to positive HV is that the readout requires capacitive coupling. Active base designs for negative and positive HV voltage have been realized and tested. The best solution to have a reduced dark rate will be adopted. On top of the HA-coating, another method, which proved very successful, was the conformal coating adopted by the KM3NeT experiment [?]. We have compared the R14374 to the HZC XP82B20 and XP72B2F PMTs. Fig. 32 shows the results for the 3 PMTs, operated in negative HV mode. One observes that the dark rate is reduced between the XP82B20 (old) and XP72B2F (new) HZC PMTs, decreasing from 1700 to 200 Hz at 13° for a 0.4 photoelectron threshold. At this temperature the XP72B2F and Hamamatsu-R14374 have similar dark rates. However, the temperature dependency of the dark rate appears to be larger for XP72B2F than for the Hamamatsu-R14374, increasing respectively to 600 Hz and 300 Hz at 20°C .

We have studied several ways to reduce the dark count rate to 100 Hz since this has a significant impact on the physics performance. We are pursuing R&D together with manufacturers, and also looking at the performance of the 3" PMTs in the Kamioka mine as compared to ground level. For the 20" PMTs a significant reduction in dark rate was found in the mine due to the lower rate of cosmic muons. The low temperature dependency of the Hamamatsu R14374 dark rate observed in Fig. 31 indicates that the dominant dark rate source may come from radioactive material in the PMT glass. The scintillation of these generates a cascade, which may lead to several dark rate counts in a narrow time window. Such cascades were measured using a flash-ADC with a $40 \mu\text{s}$ time window. Fig. 33 shows examples of a single and a cascade of dark rate counts. The number of dark rate counts in $40 \mu\text{s}$ time window, and the time difference between two consecutive dark hits are shown in Fig. 34. One

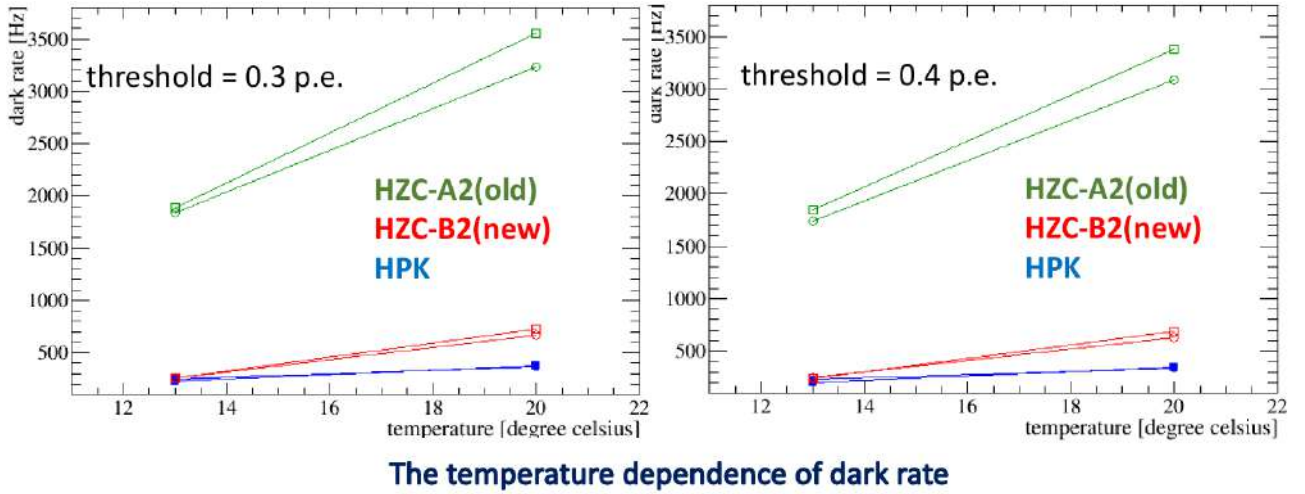


Figure 32: Dark rate of Hamamatsu R14374 (blue), XP82B20/old (green) and XP72B2F/new (red) operated at a gain of 1×10^7 in negative HV mode. The squares represents the first set of measurement, and the circles the second one to test reproducibility.

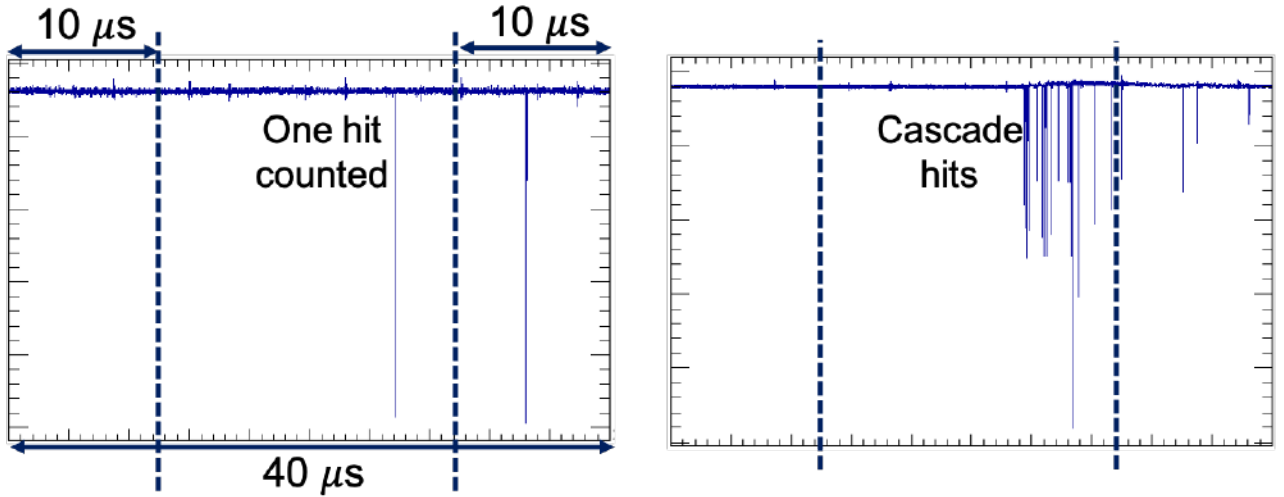


Figure 33: Data produced with a Hamamatsu R14374 PMT operated in 13°C air at -1250 V, with a threshold of 0.4 p.e. (Left) Single dark rate count event. (Right) Cascade dark rate count event.

observes that a large fraction of the events have multiple dark rate counts that have a particular time structure, mostly concentrated within a $5 \mu\text{s}$ after the previous dark hit. Such continuous dark rate hits can be reduced by masking any PMT that has two 1 p.e. signals in a chosen ΔT time window. In order to study the potential reduction in the dark rate count, we have removed events showing two consecutive hits as a function of the ΔT time window. The result shown on Fig. 35 confirms that most of the dark rate counts are clustered in a $< 5 \mu\text{s}$ time window. It also shows that, provided we mask the R14374 PMTs with two or more consecutive dark rate hits in a $5 \mu\text{s}$ time window, the dark rate can be reduced by 60% and reach values close to the required 100 Hz. We note that the probability of continuous dark rate is slightly lower for the HZC PMT than for the Hamamatsu PMT.

In conclusion we observe a similar dark count rate for the Hamamatsu R14374 and HZC XP72B2F PMTs of about 200 Hz in air at 13°C. We do not observe a significant different between positive and negative high voltage modes, but there is a small reduction using HA-coating to cover the PMT photocathode. We measured the temperature dependency of the dark count rate, and it was higher for the XP72B2F than for the R14374 PMT. We studied a method to reduce the dark rate by removing cascade dark hits by masking the PMT if it happens. If this is done the dark rate could be brought down to ~ 100 Hz at 13°C for a 0.4 p.e. threshold. Such an observation indicates that major component of the dark rate is coming from the scintillation of the glass

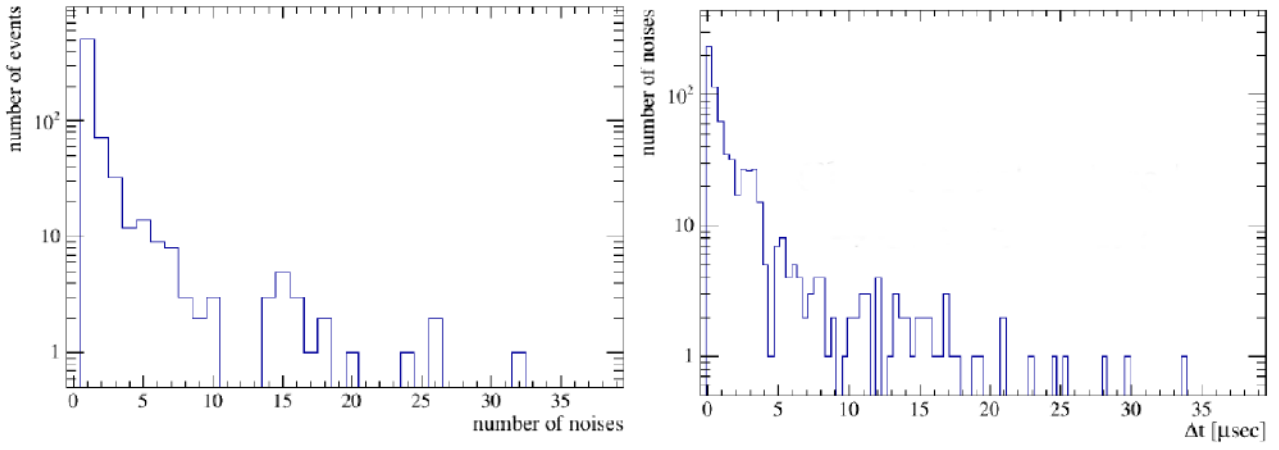


Figure 34: Data produced with a Hamamatsu R14374 PMT operated in 13°C air at -1250 V, with a threshold of 0.4 p.e. (Left) Number of dark rate counts in a 40 μ s time window. (Right) Time difference between two consecutive dark counts in the acquisition time window.

radioactive materials. The possibility of reducing this radioactive contamination in the PMT glass is being discussed with the manufacturers.

In the near future these measurements will be repeated in water, where we might observe a significant reduction of the dark rate count for the positive high voltage mode. We plan to conduct a series of experiments to decide on the treatment of the outside of the PMT and on the preferred HV polarity.

5.1 Stability of dark rate and gain

It is necessary to investigate the time stability of 3" PMT. Using the same setup in section 5, dark rates for relatively long term was measured. Fig.36 shows the dark rate as a function of minutes (left) and hours (right). Positive 1250 V is supplied to the same HA-coated PMT as that used in Fig.31. The temperature was kept at 13°C during the measurement. The dark rate seems to be stable after about an hour.

In order to check in more detail, we kept two PMTs for about 40 days at a temperature of 17°C and with - 1301 V, and measured the gain and dark rate. The setup is the same as Fig.41. Gain was measured by illuminating low intensity laser with less than 1 p.e. in average and determined by fitting the integrated charge distribution with Gaussian functions. To suppress the thermal electron emission, the gains were measured after the dark rate measurement every time. The results were shown in Fig. 37. Overall, gain and dark rate seem to be stable within 10%. In the PMT#2, the dark rate was higher immediately after the HV applied, but it decreased to the comparable rate as the PMT#1 after a few days.

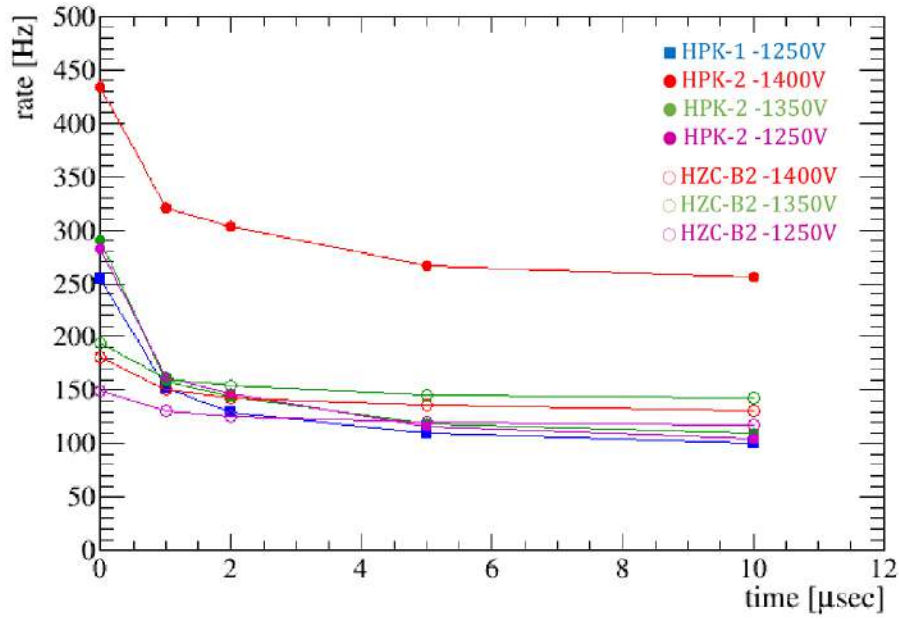


Figure 35: Dark rates with different cut conditions. Horizontal axis shows the minimum time interval of two consecutive hits to count in the dark rate. Dark rates were measured for Hamamatsu R14374 (plain circles) and HZC XP72B2F (empty circles) PMTs. PMT are operated in negative high voltage at 1250 (magenta), 1350 (green) and 1400 V (red), in a temperature of 13°C. Dark hits were counted with a threshold of 0.4 p.e.

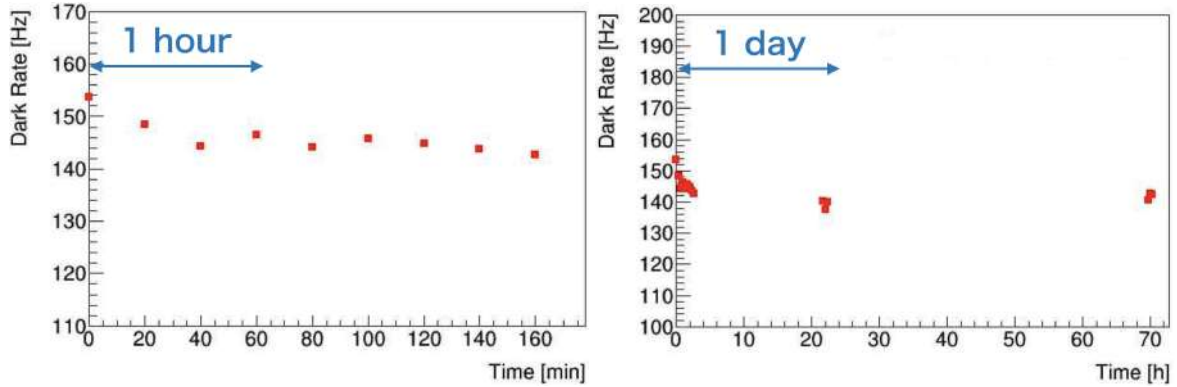


Figure 36: Time dependence of the dark rate for HA-coated 3'' PMT at a temperature of 13°C.

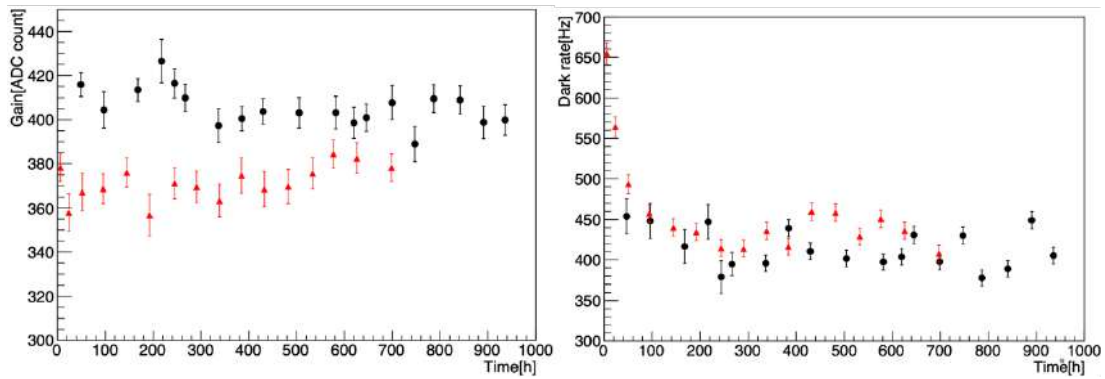


Figure 37: Time dependence of the gain (left) and dark rate (right) for two PMTs, PMT#1 with black points and PMT#2 with red points.

5.2 IWCD mPMT Dark Noise Rate Measurements

A similar set of dark noise measurements were made at TRIUMF with the IWCD revision-0 mainboard electronics. These measurements were made with Hamamatsu R14374 3" PMT with the INFN/Warsaw negative polarity active bases. We tested a mix of HA-coated and regular PMTs.

These tests were done as follows:

- The mPMT mainboard was configured to take random triggers; we took as many triggers as possible to accumulate enough statistics.
- We analyzed the waveform for each PMT to look for any pulses. We used a simple threshold cut to determine if there was a dark noise pulse.

One issue with these dark noise tests is that we have not been consistent with what threshold we were using for the pulse finding. The threshold is somewhere between 0.3PE and 0.6PE, but we can not be too certain about which exact threshold was used in all cases.

We also did tests similar to the measurements at IPMU, looking for cascade type events where a large number of hits were seen in a 10us window. We tried some tests where we would try to ignore the cascade hits by only counting a single dark noise hit in a 10us waveform. We found that this method of counting the dark noise rate was approximately 15% to 30% lower than a dark noise rate calculated by including all the hits we found. However, we did not do any detailed studies on this.



Figure 38: Setup for testing PMT dark noise rate testing. On the left is the PMTs in the environmental controlled chamber with mPMT electronics. On the right is the fully integrated mPMT, covered with light-tight wrapping.

These tests were done in two parts. First tests were done with PMTs in an environmental chamber. We could put six PMTs into the chamber at one time. A picture of the setup is shown in the left side of Figure 38.

The first test was to measure the dark noise rate as a function of temperature. We made measurements of the dark dependence between 5C and 23C. The results can be seen in Figure 39. We see the following results from this plot:

- There is no strong difference between the dark noise rate of the regular and HA-coated PMTs (though statistics are small).
- The dark noise rate is flat with temperature between 5C and 11C, but above 11C the dark noise rate seems to increase significantly with temperature.

We also found that there was no difference in the dark noise rate when other PMTs were turned on or off. Ie, if we turned off 5 of the 6 PMTs in the chamber, the dark noise rate of the last PMT did not obviously change. This suggest that there is not significant rates of flashes in one PMT that cause dark noise hits in other PMTs.

The second test was done with a fully integrated mPMT module (seen in the right side of Figure 38). The integration mPMT had 17 real PMTs, but only 12 PMTs were turned on and used in the test described here.

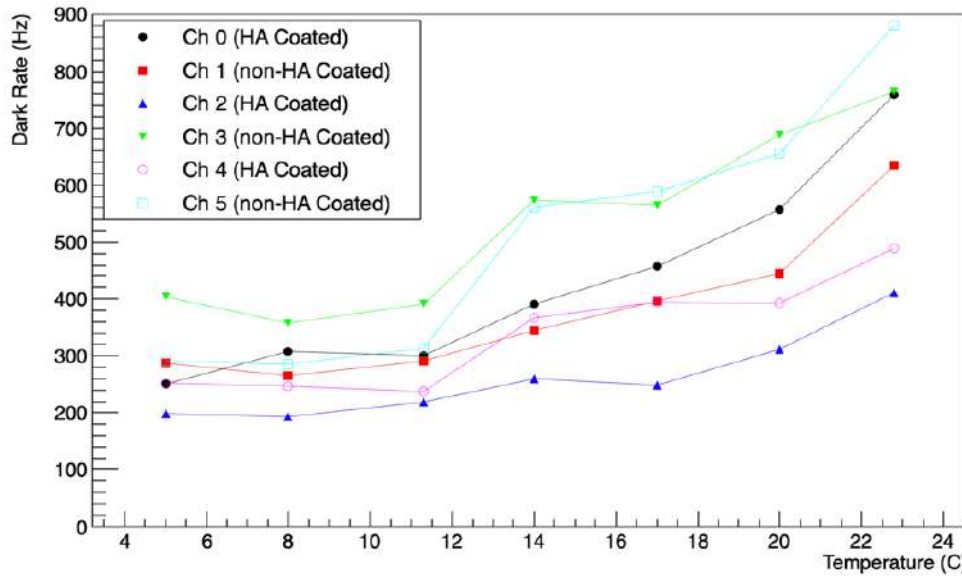


Figure 39: Figure shows the dark noise rate versus temperature for 6 PMTs in the environmentally controlled chamber.

One of the challenges with the tests with the integration mPMT was the cooling of the mPMT. For this test we cooled the mPMT backplate with a copper cooling block, which was cooled by 12C water. We used additional thermocouples to measure the temperatures at various points around the mPMT. We eventually got the temperature of the PMTs down to approximately 23C.

One observation was that the dark noise rates took a long time to stabilize after the PMTs had been exposed to light. Figure 40 shows the dark noise rate of the 12 PMTs over approximately 1 month in May and June 2021. As you can see, there is a large drop in the measured dark noise rate over the first 5 days, but then a longer, slower reduction in the dark noise rate over the next 20-30 days.

In Figure 40 one can also see that there are significant jumps in the dark noise rate for particular periods; these periods are strongly correlated with jumps in the measured PMT temperatures on particularly hot days in the lab. This seems further evidence that, at these temperatures, the dark noise rates are strongly dependent on temperature.

Finally, Figure 40 shows that, after stabilization, the PMT dark noise rates for the integration mPMT get down into the 300-1200Hz range. This is a higher dark noise rate than we want for the mPMTs. But this range of temperature is consistent with the range of dark noise rates that we would expect when the PMTs are operating at 23C, at least according to Figure 39.

A summary of all the measurements with the revision-0 mPMT mainboard is shown in Table 2.

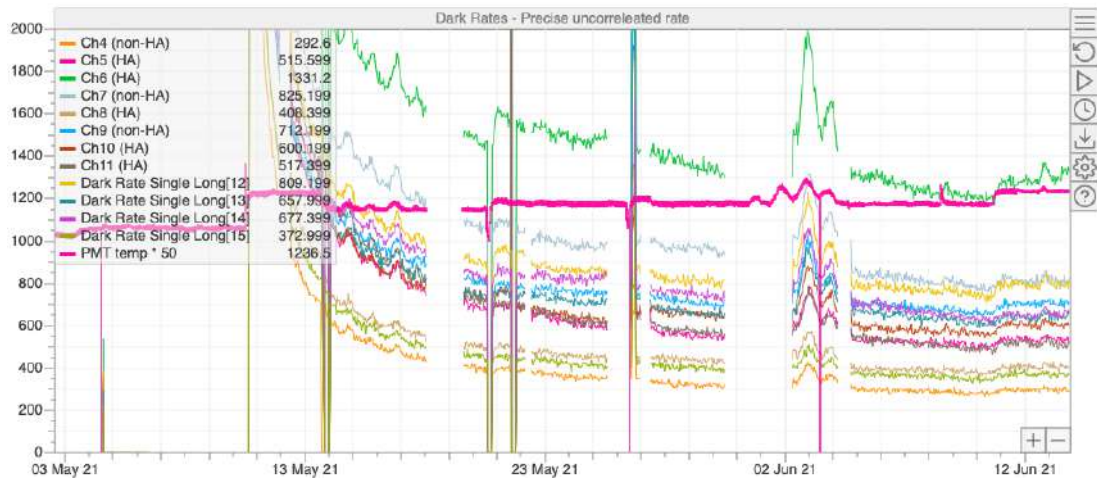


Figure 40: Figure shows the dark noise rate vs time for 12 PMTs in the integration mPMT during May and June 2021. There are gaps in the dark noise rate measurements when data taking was interrupted. The thicker pink link is correlated with the PMT temperature; specifically it is the PMT temperature * 50.

PMT Type	Serial Number	Dark Rate (Hz)		
		Individual Setup 13C	Integrate mpMT 17C	Integrate mpMT 23C
Normal	KM09817	300 ± 2	310 ± 5	390 ± 20
normal	KM14449	450 ± 4	510 ± 6	X
normal	KM09823	320 ± 2	380 ± 5	X
HA-coated	KM11968	200 ± 2	220 ± 5	730 ± 20
HA-coated	KM13040	240 ± 2	260 ± 5	X
HA-coated	KM12983	300 ± 2	360 ± 5	X
HA-coated	KM12200	310 ± 2	395 ± 5	320 ± 20
HA-coated	KM12340	308 ± 2	410 ± 2	X
HA-coated	KM12944	260 ± 2	320 ± 5	1300 ± 20
HA-coated	KM12942	390 ± 2	445 ± 5	540 ± 20
HA-coated	KM12925	288 ± 2	360 ± 5	X
HA-coated	KM12946	214 ± 2	250 ± 5	X
HA-coated	KM12918	X	X	930 ± 20
HA-coated	KM12922	X	X	430 ± 20
HA-coated	KM11950	X	X	690 ± 20
HA-coated	KM11985	X	X	630 ± 20
HA-coated	KM11932	X	X	590 ± 20
HA-coated	KM12923	X	X	820 ± 20
HA-coated	KM12926	X	X	650 ± 20

Table 2: Table shows the dark noise rate measured for various PMTs in the two different setups; the individual PMT measurements in the environmentally controlled chamber and the measurements in the fully integrated mPMT. X indicated that measurements were not taken with that PMT in a particular setup.

6 Afterpulse Measurements

In addition to the dark-rate measurement, we also measured after-pulse of 3" PMT. The after pulse is the fake noise pulse appearing after the signal pulse with delay ranging up to $\mathcal{O}(10^{-6})$ s. As the mechanism, the residual gases inside 3" PMT are ionized by primary photoelectrons, and the positive ions drift back and strike the photocathode, which leads to generate secondary electrons. The delay time from the main pulse and amplitude of after pulse varies depending on a PMT operation condition such as dimension of PMT or types of residual gases and ionized nuclei. High rate after-pulse could become a source of background for the physical process such as decay Michel electron tagging and neutron capture tagging. The 3" PMT photocathode was illuminated by optical laser oscillator, and Flash-ADC recorded the waveforms shown in Fig. 41 as same as dark-rate measurements. We measured after-pulse for the Hamamatsu R14374, HZC XP82B20 and HZC XP72B2F PMTs. The height threshold for after-pulse is set to be 0.35 p.e..

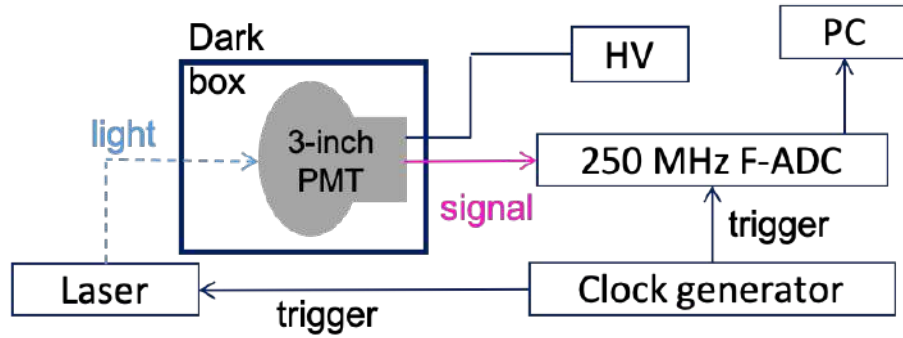


Figure 41: Schematics of the after pulse measurement setup of the 3" PMT

Fig. 42 shows the height of after-pulse and the time intervals between the main pulse and after-pulse. We found that each types of 3" PMT has one p.e. level signals 2-4 μ s later from the main signals. Comparing to the dark signals scaled with measurement time shown in Fig.43, there was no significant excess due to after pulses with a time interval of more than 10 μ sec.

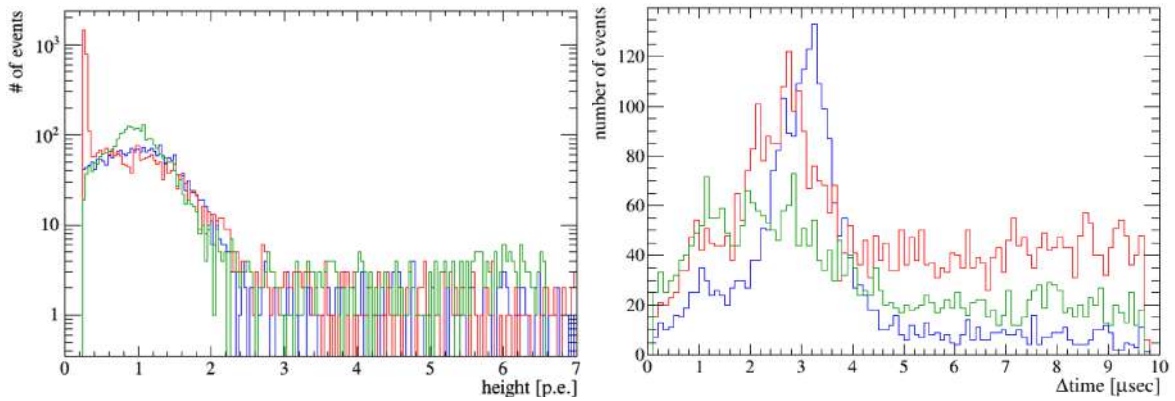


Figure 42: The height of after pulses (left), and the time intervals between the main pulse and after pulse (right). Hamamatsu (blue), HZC XP72B2F (red) and HZC XP82B20 (green). PMTs are compared in the plots.

Fig. 44 shows the relation between the magnitude of main pulse and after pulse occurrence, because the after-pulse is caused by photoelectrons of main signal. Each plot shows the fraction of events with after pulse as a function of the first pulse height and integrated charge.

The fraction of Hamamatsu R14374 is proportional to main pulse height and integrated charge, but on the other hand, that of both HZC PMTs is much smaller. In conclusion we observe 1 p.e level after pulse signals at 2-4 μ s later from the main pulse. After pulses were confirmed in both Hamamatsu and HZC PMTs, but the after pulse fraction is different between them.

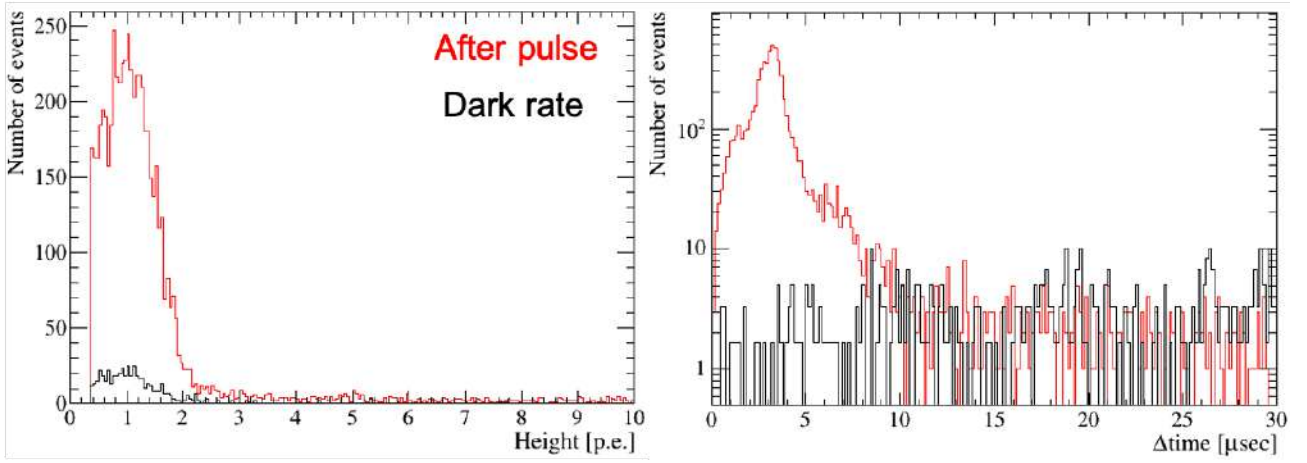


Figure 43: Pulse height (left) and time interval between the main pulse and after pulses (right) for the after pulse signals with the main pulse from laser light (red) and dark noise hits without laser light (black).

6.1 After-pulse measurements using IWCD mPMT's rev. 1 mainboard

A similar after-pulse rate study was performed using the rev. 1 mainboard for IWCD's mPMT. The experimental set-up consisted of four Hamamatsu R14374 PMTs connected to different channels of 125-MSPS quad-channel analog-to-digital converters (ADC) on the mainboard. A pulser generated a trigger for both the digitizers and a Tamadenshi laser, which hit the four PMTs simultaneously through a diffuser. The after-pulse rate measurement then followed as: collection of a considerable number of waveforms containing the laser signals and after-pulses; of the number of pulses in the waveforms, using the PTF analysis code and the simple-threshold pulse-finding technique; and the estimation of the after-pulse rate, which considered the height of the laser signal and the number of consequent after-pulses. The PMT's high-voltage supply and the laser's intensity were then adjusted so that the PMTs' gain equalization yielded the desired single photo-electron (p.e.) pulse height of 8 mV. It is likely that the PMTs were running at $\sim 3 \times 10^7$ gain, but it is not confirmed.

To identify laser pulses (prompt signals) apart from the after-pulses in waveform, a simple time window was used; the prompt signal was taken as the first pulse in the interval of 2210 ns to 2220 ns, and every following pulse was counted as after-pulse. Waveforms with a pulse earlier than 2210 ns were discarded. After finding the laser pulse, it was categorized into levels multiple of 0.5 p.e., and for each of these p.e. levels, after-pulse rate R was calculated as

$$R = \frac{N_{\text{afp}}}{N_{\text{laser}}} \cdot 100\% \quad (9)$$

N_{afp} is the total number of after-pulses in the data set at said p.e. level and N_{laser} is the respective total number of lasers pulses. In fact, N_{textafp} was determined in two ways: by counting only a single afterpulse per the waveform, or by counting all the afterpulses in the waveform. Explicitly,

$$R_{\text{single}} = \frac{(\text{sum of every event with afterpulse})}{N_{\text{laser}}} \cdot 100\% \quad R_{\text{all}} = \frac{(\text{sum of every afterpulse})}{N_{\text{laser}}} \cdot 100\% \quad (10)$$

Waveforms with a pulse earlier than 2210 ns were used for a preliminary dark-count rate (DCR) estimation. These early pulses were counted, divided by the early time window (2210 ns) and averaged over all waveforms in the data set. From the average, $\langle \text{DCR} \rangle$, we estimated the average number of dark pulses per waveform, which we then subtracted from the N_{afp} count, to determine a DCR-corrected value for the afterpulse rate.

For run 400, 999, 974 waveforms were collected for each of the four PMTs/channels. The distribution of pulse height and timing is found in Fig. 45, along with their respective timing distribution subtracted by 2210 ns. Our final results, for the original and DCR-corrected after-pulse rates are shown in Fig. 46. The functional form and fitting parameters are in table 3, with $\langle \text{DCR} \rangle$. Notice how the afterpulse rate, counting all after-pulse events in the waveform, increases linearly with prompt signal's height. After applying the DCR correction, their vertical offsets decrease. In turn, the number of waveforms containing at least one after-pulse increases with a power of the prompt signal's height. Please refer to our technical report for more details, including pulse-finding efficiency estimations.

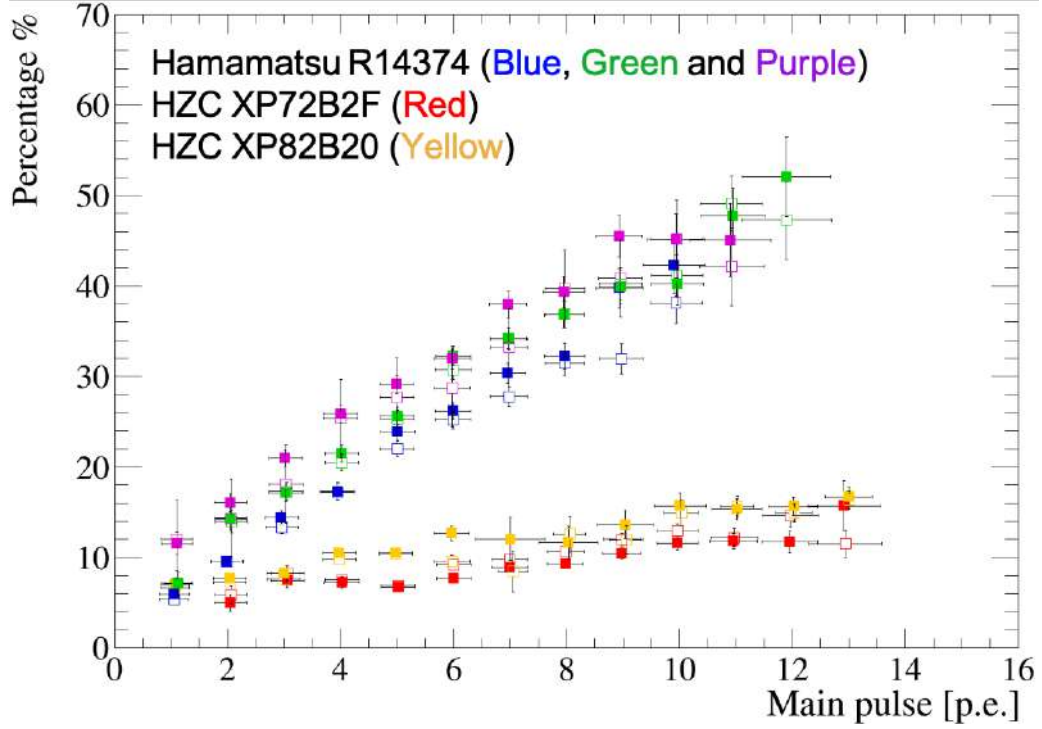


Figure 44: Fraction of the events with after pulse for Hamamatsu and HZC PMTs. Filled points show the fraction as a function of the main pulse height, and empty points show that of integrated charge.

	Red curve: $y(x) = mx + c$			Blue curve: $y(x) = mx + c$			Green curve: $y(x) = mx^n + c$		
	m (%/p.e.)	c (%)		m (%/p.e.)	c (%)	$\langle \text{DCR} \rangle$ (Hz)	m (%/p.e. ^{n})	n	c (%)
0	11.88 ± 0.05	4.3 ± 0.2		11.91 ± 0.05	2.0 ± 0.2	2820 ± 40	20.3 ± 0.9	0.57 ± 0.02	-7 ± 1
1	10.24 ± 0.05	7.9 ± 0.5		4.5 ± 0.4	1.03 ± 0.02	3800 ± 40	85 ± 20	0.23 ± 0.04	-80 ± 20
2	7.54 ± 0.03	4.2 ± 0.1		7.55 ± 0.03	0.79 ± 0.09	4060 ± 40	9.3 ± 0.4	0.74 ± 0.02	0.5 ± 0.5
3	5.46 ± 0.03	9.7 ± 0.1		5.55 ± 0.01	-2.31 ± 0.01	14260 ± 80	6.0 ± 0.3	0.80 ± 0.02	7.4 ± 0.5

Table 3: Fitting parameters for curves in Fig 46.

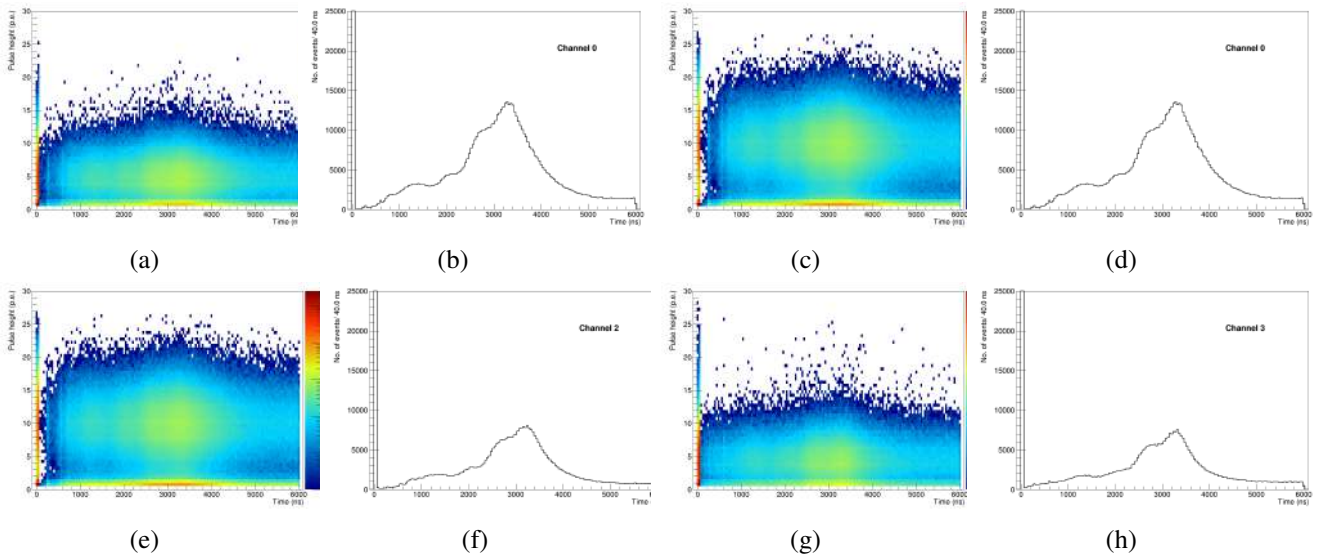
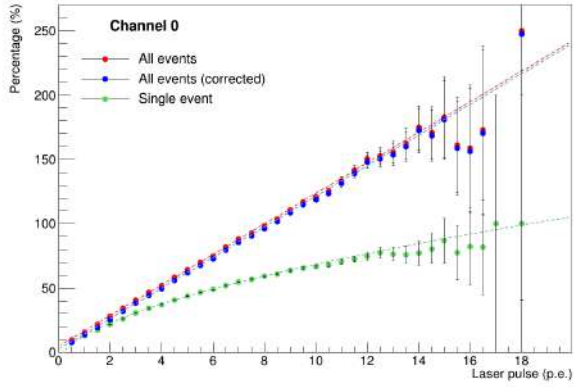
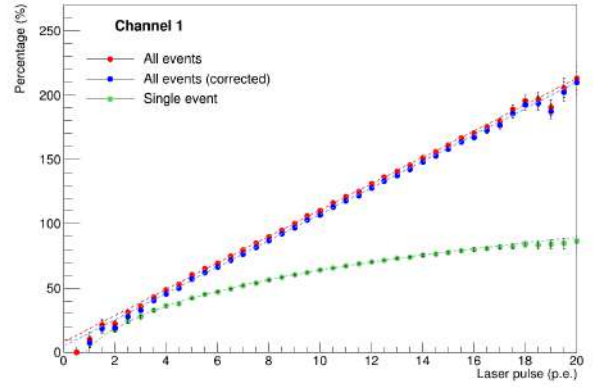


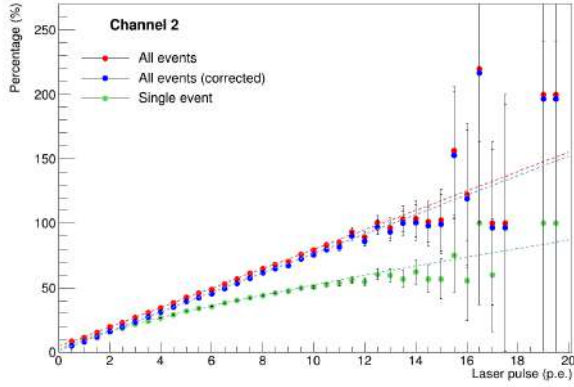
Figure 45: Run 400. Distributions of pulse amplitudes and pulse timing for laser pulse at zero: (a) and (b) Channel 0, (c) and (d) Channel 1, (e) and (f) Channel 2, and (g) and (h) Channel 3.



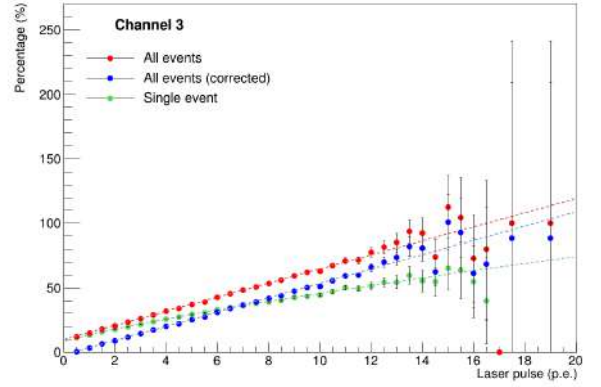
(a)



(b)



(c)



(d)

Figure 46: Run 400. Afterpulse rates for: (a) Channel 0, (b) Channel 1, (c) Channel 2 and (d) Channel 3. Red curves are the R_{all} afterpulse rate and green curves are the R_{single} afterpulse rate. The fitting functional form and parameters are in table 3.